



AMERICAN METEOROLOGICAL SOCIETY

Monthly Weather Review

EARLY ONLINE RELEASE

This is a preliminary PDF of the author-produced manuscript that has been peer-reviewed and accepted for publication. Since it is being posted so soon after acceptance, it has not yet been copyedited, formatted, or processed by AMS Publications. This preliminary version of the manuscript may be downloaded, distributed, and cited, but please be aware that there will be visual differences and possibly some content differences between this version and the final published version.

The DOI for this manuscript is doi: 10.1175/MWR-D-17-0080.1

The final published version of this manuscript will replace the preliminary version at the above DOI once it is available.

If you would like to cite this EOR in a separate work, please use the following full citation:

Portele, T., A. Dörnbrack, J. Wagner, S. Gisinger, B. Ehard, P. Pautet, and M. Rapp, 2018: Mountain Wave Propagation under Transient Tropospheric Forcing A DEEPWAVE Case Study. *Mon. Wea. Rev.* doi:10.1175/MWR-D-17-0080.1, in press.

© 2018 American Meteorological Society



Mountain Wave Propagation under Transient Tropospheric Forcing

A DEEPWAVE Case Study

Tanja C. Portele*, Andreas Dörnbrack, Johannes S. Wagner, Sonja Gisinger, Benedikt Ehard,
Pierre-Dominique Pautet†, and Markus Rapp

Institut für Physik der Atmosphäre, Deutsches Zentrum für Luft- und Raumfahrt,

Oberpfaffenhofen, Germany

*Corresponding author address: Institut für Physik der Atmosphäre, Deutsches Zentrum für Luft- und Raumfahrt, Oberpfaffenhofen, Germany.

E-mail: tanja.portele@dlr.de

†Center for Atmospheric and Space Sciences, Utah State University, Logan, UT, 84322

ABSTRACT

11 The impact of transient tropospheric forcing on the deep vertical moun-
12 tain wave propagation is investigated by a unique combination of in-situ and
13 remote-sensing observations and numerical modeling. The temporal evolu-
14 tion of the upstream low-level wind follows approximately a \cos^2 shape and
15 was controlled by a migrating trough and connected fronts. Our case study
16 reveals the importance of the time-varying propagation conditions in the up-
17 per troposphere, lower stratosphere (UTLS). Upper-tropospheric stability, the
18 wind profile as well as the tropopause strength affected the observed and sim-
19 ulated wave response in the UTLS. Leg-integrated along-track momentum
20 fluxes ($-MF_{track}$) and amplitudes of vertical displacements of air parcels in
21 the UTLS reached up to 130 kN m^{-1} and 1500 m, respectively. Their maxima
22 were phase-shifted to the maximum low-level forcing by ≈ 8 h. Small-scale
23 waves ($\lambda_x \approx 20 - 30$ km) were continuously forced and their flux values de-
24 pended on wave attenuation by breaking and reflection in the UTLS region.
25 Only maximum flow over the envelope of the mountain range favored the ex-
26 citation of longer waves that propagated deeply into the mesosphere. Their
27 long propagation time caused a retarded enhancement of observed meso-
28 spheric gravity wave activity about 12 to 15 h after their observation in the
29 UTLS. For the UTLS, we further compared observed and simulated MF_{track}
30 with fluxes of 2D quasi-steady runs. UTLS momentum fluxes seem to be
31 reproducible by individual quasi-steady 2D runs except for the flux enhance-
32 ment during the early decelerating forcing phase.

33 **1. Introduction**

34 Mountain waves under transient tropospheric forcing conditions were frequently observed dur-
35 ing the DEEP propagating gravity WAVE experiment (DEEPWAVE) in austral winter 2014 (Fritts
36 et al. 2016). These events occurred episodically and were associated with migratory low-pressure
37 systems impinging the South Island (SI) of New Zealand (NZ; Gisinger et al. 2017). During these
38 events, the conditions for wave excitation and propagation varied temporally. Continuous ground-
39 based lidar observations in the lee of New Zealand’s Alps during DEEPWAVE revealed enhanced
40 gravity wave activity in the stratosphere and mesosphere which last about one to three days and
41 alternate with quiescent periods (Kaifler et al. 2015). The gravity wave forcing due to passing
42 weather systems, the appearance of tropopause jets, and the middle atmosphere wave response
43 were all observed with a similar frequency and duration of 2 to 4 days (Fritts et al. 2016; Gisinger
44 et al. 2017).

45 The episodic nature of mountain wave events due to traversing cyclones was already observed
46 during the Mesoscale Alpine Programme (MAP) and the Terrain-induced Rotor EXperiment (T-
47 REX, Smith et al. 2007; Grubišić et al. 2008; Strauss et al. 2016). During T-REX, the transient
48 formation of rotors and lee waves was investigated (Kühnlein et al. 2013), as well as the onset of
49 downslope wind storms with shifting wave patterns aloft (Strauss et al. 2016). During both field
50 campaigns the observations focused on processes within the troposphere, including the boundary
51 layer. Deep propagation of mountain waves was almost impossible during MAP, as directional
52 wind shear in the mid-troposphere acted like a critical level, except for above the western Alpine
53 Arc (Smith et al. 2007).

54 The design of DEEPWAVE allowed, inter alia, to measure orographically induced gravity waves
55 from their excitation over the mountains of the Southern Alps up to their dissipation in the middle

56 atmosphere (Fritts et al. 2016; Bramberger et al. 2017). The SI of NZ is located at about 45° S, just
57 between the polar front jet to the south and the subtropical jet to the north. The frequent appearance
58 of frontal systems allows one to study the transient forcing conditions for mountain wave excitation
59 and their impact on the gravity wave activity in the middle atmosphere. The nearly unidirectional
60 westerly winds from the troposphere to the stratosphere during austral winter are strong enough
61 that total critical levels are unlikely (Kim et al. 2003; Fritts et al. 2016). For an inviscid, adiabatic,
62 non-rotating, steady, Boussinesq flow across mountains, linear theory gives total critical levels
63 whenever the scalar product of horizontal wind (u, v) and horizontal wave vector (k, l) is zero for
64 all wavenumbers (Teixeira 2014). Thus, the DEEPWAVE campaign offered the opportunity to
65 study transient tropospheric forcing and the corresponding deep atmospheric wave response for
66 the first time.

67 The steady-state assumption is the basis of linear mountain wave theory (Smith 1979). More-
68 over, there are numerous numerical studies about transiently forced mountain waves. Lott and
69 Teitelbaum (1993a,b) investigated the wave dynamics in a 2D linear time-dependent model with
70 transient incident stably-stratified flow. Chen et al. (2005, 2007) and Hills and Durran (2012)
71 extended the work of Lott and Teitelbaum (1993a,b) and studied the impact of the flow of a time-
72 dependent barotropic planetary square wave in a uniformly stratified atmosphere over an isolated
73 3D mountain in idealized numerical simulations. Martin and Lott (2007) further addressed the
74 large-scale effect of inertia-gravity wave generation due to the passage of an idealized front over a
75 3D mountain range. Recently, Menchaca and Durran (2017) simulated an idealized cyclone pass-
76 ing an isolated ridge in a baroclinically unstable environment and investigated the wave structures
77 and the flow morphologies in the course of the idealized event. Lott and Teitelbaum (1993a,b),
78 as well as Chen et al. (2005, 2007) and Hills and Durran (2012) prescribed the cross-mountain
79 wind variation during 2 and up to 8 days with cosine-functions, increasing the wind from zero to

80 a maximum of 20 m s^{-1} and returning to zero afterwards. With such a time-varying incident flow,
81 hydrostatic wave perturbations appeared no longer over the mountains, but were shifted down-
82 stream or upstream under accelerating or decelerating forcings, respectively. For low mountains,
83 wave momentum flux was accumulated during accelerating forcing due to conservation of wave
84 action. In contrast, the flow over higher mountains generated gravity wave breaking at lower
85 levels. Here, the accumulated maximum of the zonal momentum flux during the high-drag state
86 occurred shortly after the time of maximum wind.

87 So far, no real-world case studies exist investigating a mountain wave field excited by transient
88 low-level forcing and propagating into the middle atmosphere. In this case study, a mountain wave
89 event which occurred in the period of 28 June to 1 July 2014 (intensive observing period, IOP 9)
90 is investigated. The overall questions are: (1) Which tropospheric and stratospheric quantities
91 control the transience of the event? (2) How do flux values, wave amplitudes and wave scales in
92 the upper troposphere, lower stratosphere (UTLS) respond to the varying conditions? (3) Does the
93 transient tropospheric forcing favor the excitation of certain horizontal wavelengths? (4) Can the
94 wave response in the UTLS be described by a sequence of individual steady states? (5) How does
95 the transient low-level forcing affect the wave activity in the mesosphere?

96 The paper is structured as follows: First, a description of the used dataset and the applied meth-
97 ods is given in Section 2. The following Section 3 provides a detailed description of the me-
98 teorological evolution during the intensive observing period (IOP) 9. The results are presented
99 separately for the wave response in the UTLS (Section 4a) and for the deep vertical wave prop-
100 agation into the mesosphere (Section 4b). The findings are discussed and related to literature in
101 Section 5. The research questions are answered in Section 6. The Appendix gives an overview of
102 the extended wavelet transform used in this paper.

103 **2. Methodology**

104 IOP 9 took place from 28 June till 01 July 2014. Altogether, six coordinated flights of the
105 NSF/NCAR Gulfstream V (GV, RF11 - RF14) and the DLR research aircraft Falcon (FF01 and
106 FF02) were conducted. During IOP 9, different flight patterns were flown (Fig. 1). Flight altitudes
107 and times can be extracted from Fig. 2.

108 The analysis presented in this paper focuses on observations along the Mt.-Aspiring-2b transect
109 (Fig. 1), a mountain wave flight track with a direction of 300 degrees from NW to SE over the
110 Mount Aspiring (44.38° S, 168.73° E). During IOP 9, a total flight duration of 9.5 hours was spent
111 along this transect comprising 19 flight legs (RF 12: 6 legs, FF 01: 3 legs, RF 13: 6 legs, FF 02:
112 4 legs). One flight leg (FF01 leg 1) was flown along a slightly shifted flight track compared to
113 the Mt.-Aspiring-2b transect (thin red line in Fig. 1) and is only included in the analysis where
114 specifically stated.

115 The topography of the SI is rough and structured with a sequence of valleys oriented parallel to
116 mountain range. Along the Mt.-Aspiring-2b transect, several individual peaks can be identified.
117 These peaks are labelled in Fig. 3a and their respective names, latitudes and longitudes are listed
118 in Table 1. Their positions on the map can be found in Fig. 3b. Mt. Aspiring is the highest peak
119 along this track. The outstanding peak at 20 km distance belongs to the Dunstan Mountains in
120 Central Otago, located directly upstream of the radiosonde and Rayleigh lidar station in Lauder
121 (Fig. 1). All GV flight legs were flown within the stratosphere at around 12 and 14 km altitude,
122 whereas the Falcon crossed the tropopause during both FF01 and FF02 (Table 2, Fig. 2).

123 For this study, the 1-Hz in-situ flight-level data of the GV and Falcon were used. For the GV,
124 general measurement uncertainties are given in Smith et al. (2016). For the Falcon, measure-
125 ment uncertainties can be found in Rotering (2011) and Giez et al. (2017). Only GPS height data

126 (no differential GPS) are available for the Falcon during the DEEPWAVE campaign. Onboard the
127 GV, upper atmosphere observations were performed using an Advanced Mesospheric Temperature
128 Mapper (AMTM) imaging system. This instrument measures the intensity and rotational tempera-
129 ture of the bright OH airglow layer located at ≈ 87 km altitude. In statistical thermodynamics, the
130 rotational temperature is the temperature at which the thermal population of the rotational states is
131 such as to give rise to the observed rotational spectrum, in terms of the relative intensities of the
132 different transitions. The equivalence of the OH rotational temperature and the temperature of the
133 emitting atmosphere, established by Wallace (1962), allows to measure the mesopause tempera-
134 ture at the altitude of the OH airglow layer. Therefore, this emission has been extensively used to
135 study waves propagating through the mesosphere lower thermosphere (MLT) region (e. g. Pautet
136 et al. 2014; Bossert et al. 2015; Pautet et al. 2016; Eckermann et al. 2016).

137 Altogether 23 radiosondes were launched from Haast on the upstream side of the Southern Alps
138 and from Lauder in the lee of the main ridge of the Southern Alps. The locations of radiosonde
139 stations and the balloon trajectories are given in Fig. 1. These soundings (8 from Haast and 15
140 from Lauder) complemented the airborne measurements with respect to vertical observations from
141 the ground up to the stratosphere. A maximum altitude of 36 km was achieved and the average
142 flight duration was 2.5 hours.

143 In addition, DLR operated a mobile middle-atmosphere Rayleigh lidar at Lauder. On the basis
144 of integrated range-corrected photon count profiles (which are proportional to atmospheric den-
145 sity profiles), temperatures are retrieved assuming hydrostatic equilibrium. Temperature profiles
146 are available from the middle stratosphere at about 30 km up to around 80 km altitude in the
147 mesosphere. Details of the instrumentation of the lidar can be found in Kaifler et al. (2015). Mea-
148 surement uncertainties, as well as the calculation of the temperature perturbations T' applying a
149 Butterworth filter are described in Ehard et al. (2015). During IOP 9, the lidar operated exclusively

150 during the entire night of 30 June 2014. The determination of the averaged gravity wave potential
151 energy density (GWPED) in the upper stratosphere (28 - 44 km), stratopause (44 - 60 km) and
152 mesosphere (60 - 76 km) as a measure of the gravity wave activity in the three altitude ranges
153 is explained in Kaifler et al. (2015). Here, a 1-h running mean of the 2-min vertically averaged
154 observational data is calculated.

155 Six hourly operational analyses valid at 00, 06, 12, and 18 UTC and 1-hourly high-resolution
156 forecasts at intermediate lead times (+1, +2, +3, +4, +5, +7, +8, +9, +10, +11 h) of the 00 and
157 12 UTC forecast runs of the integrated forecast system (IFS) of the European Centre for Medium-
158 Range Weather Forecasts (ECMWF) are further used to visualize the temporal evolution of the
159 upstream conditions at 44.20° S, 167.50° E (Fig. 1). The IFS Cycle 40r1 has a horizontal res-
160 olution of about 16 km, 137 vertical model levels and a model top at 0.01 hPa, with numerical
161 damping starting at 10 hPa (Jablonowski and Williamson 2011).

162 Moreover, mesoscale numerical simulations with the Weather Research and Forecasting (WRF¹,
163 Skamarock et al. 2008; Skamarock and Klemp 2008) model are performed. With the use of Ad-
164 vanced Research WRF version 3.7, atmospheric simulations are generated processing operational
165 ECMWF analyses as initial and boundary conditions. Two nested model domains are centered at
166 43° S and 169° E over the SI of NZ. The inner domain has a horizontal resolution of 2 km with
167 553 x 505 grid points in the x-y plane and the outer domain a resolution of 6 km with 440 x 430
168 grid points. 138 terrain-following levels are used in the vertical with level distances stretching
169 from 85 m near the surface to about 170 m at 1 km altitude. Level distances are kept nearly con-
170 stant at 170 m in the troposphere. Above 10 km altitude they are further stretched from 170 m to
171 1.5 km at the model top, which is set at 2 hPa (about 40 km). Implicit damping of the vertical
172 velocity (Rayleigh damping layer, Klemp et al. 2008) is applied to the uppermost 7 km of the

¹Freely available: http://www2.mmm.ucar.edu/wrf/users/download/get_source.html

173 model domain. This damping layer impedes wave reflection at the model top. The flow structure
174 up to 25 km altitude is only marginally influenced when using damping layers of 10 km and 15 km
175 thickness (not shown). The WRF simulations are initialized at 18 UTC on 28 June 2014 with IFS
176 operational analyses and are run for 54 hours until 00 UTC on 1 July 2014. The usefulness of
177 the combination and comparison of the high-resolution output of the WRF simulations with lidar,
178 aircraft and radiosonde data was already demonstrated by Ehard et al. (2016) and Wagner et al.
179 (2017).

180 To investigate the flow development along the Mt.-Aspiring-2b cross section under quasi-steady
181 background conditions, six simulations are performed with the WRF model in a two dimensional
182 idealized set up covering the core period of the transient event. The model domain has a horizontal
183 extent of 400 km and a model top at 40 km. The same vertical levels as in the real case simulations
184 are used and the lower boundary is defined by the topography along the Mt.-Aspiring-2b cross sec-
185 tion. These runs are initialized with vertical profiles of horizontal wind and potential temperature
186 taken at the first upstream point of the Mt.-Aspiring-2b cross section from the innermost domain
187 of the transient simulation. The six upstream profiles are taken every 6 hours between 00 UTC
188 on 29 June and 06 UTC on 30 June and are kept constant throughout each simulation covering
189 48 hours. In the 2D WRF model open boundary conditions are used in flow direction. Note that
190 horizontal winds are projected to a wind direction of 300 degree (u_{track}), which is the direction
191 of the Mt.-Aspiring-2b transect (Fig. 1). All idealized simulations are run without moisture and
192 radiation effects.

193 From both the WRF and the in-situ flight level data, vertical energy and momentum fluxes are
194 calculated according to the method of Smith et al. (2008) with a leg integration of $p'w'$ (EF_z),
195 $u'w'$ (MF_x), $v'w'$ (MF_y) and $u'_{track}w'$ (MF_{track}) in units of $W m^{-1}$ and $N m^{-1}$, respectively. The
196 perturbation quantities of wind (u' , v' , w') and pressure (p') are calculated by detrending the data

197 of each leg and removing the mean over the leg. The detrending is performed by subtracting a
198 linear least-square fit. Before detrending, the pressure is corrected for altitude changes (Smith
199 et al. 2008). The detrending of p corresponds to a geostrophic correction (Smith et al. 2016).
200 Detrending of the wind variables is especially necessary for legs where synoptic-scale systems
201 may cause gradients. For the in-situ flight level data, a wavelet analysis is further performed to
202 quantify gravity wave propagation both spatially and spectrally. In extension to the approach of
203 Woods and Smith (2010a,b), the energy and momentum flux cospectra are reconstructed in such a
204 way that the integrated cospectra directly result in the leg-integrated flux values obeying the correct
205 units. This extended wavelet transform and the calculation of significant parts of the cospectra are
206 described in more detail in the Appendix.

207 **3. Meteorological Evolution during IOP 9**

208 The tropospheric flow during IOP 9 started as a so-called trough-north-west regime character-
209 ized by a low-level northwesterly flow (28–30 June 2014) and proceeded to a trough regime with
210 more westerly low-level flow on 1 July 2014 (Gisinger et al. 2017, Table 1, Fig. 2g). Figure 4
211 illustrates the eastward propagation of a Rossby wave train by means of the 700 hPa meridional
212 wind component v averaged between 40° S and 45° S. During the period from 28 to 29 June 2014
213 v swapped sign from positive to negative over the SI. This indicates the passing ridge axis prior
214 to the trough in the west. This transition caused increasing north-westerly and westerly winds
215 associated with a passing occluding frontal system (Fig. 5a, b). On 29 June at 12 UTC, a broad
216 band of horizontal winds $V_H > 20 \text{ m s}^{-1}$ was directed almost perpendicular to the mountain range
217 of the SI (Fig. 5b). In the following 24 hours, the wind direction stayed nearly constant at 700 hPa
218 but V_H decreased in magnitude as displayed in Figures 5d and 5f. The cold front associated with
219 the slowly eastward migrating trough reached the SI at 700 hPa on 30 June at 12 UTC (Fig. 5e).

220 According to Fig. 4, the northerly component of the tropospheric flow lasted until 1 July 2014.
 221 Afterwards, the meridional wind component v became positive again, indicating the passage of the
 222 trough axis and the transition to southwesterly winds.

223 In Figure 6, the time series of the IFS upstream cross-mountain wind component (U_{\perp} , direc-
 224 tion $\approx 322^{\circ}$) averaged over the lowest 4 km of the troposphere is shown together with radiosonde
 225 observations from Haast and Lauder for the four-day period of IOP 9. The cross-mountain wind
 226 direction matches the mean wind direction at low levels below crest height and is therefore also
 227 approximately the wave vector direction. The cross-mountain winds increased from about 2 m s^{-1}
 228 up to 22 m s^{-1} from 00 UTC on 28 June 2014 until 10 UTC on 29 June 2014 and decreased almost
 229 down to the initial value thereafter (Fig. 6). The radiosonde cross-mountain winds generally fol-
 230 low the course of the IFS time series. However, larger deviations occurred during 30 June 2014.
 231 These deviations can be explained by the cold front approaching from the west (Fig. 5e) and pass-
 232 ing first the upstream point, then Haast and last Lauder, causing winds to decrease at Haast and
 233 Lauder later in time.

234 From Fig. 6, it is found that IOP 9 is centered around a strong forcing period of $U_{\perp} > 15 \text{ m s}^{-1}$
 235 between 02 UTC and 20 UTC on 29 June 2014 (maximum forcing phase). Before and after,
 236 weak to moderate cross-mountain winds ranging up to 5 and 15 m s^{-1} , respectively, define the
 237 accelerating and decelerating forcing phases of this transient event. The evolution of the cross-
 238 mountain wind U_{\perp} can be approximated by $U_{\perp}(t) = U_{\perp 0} + \Delta U_{\perp} \cos^2(\pi t / t_{tot})$, which is shown as
 239 dashed line in Fig. 6. Here, $U_{\perp 0} = 5 \text{ m s}^{-1}$ is the value at the beginning and at the end of the
 240 transient event, $\Delta U_{\perp} = 17 \text{ m s}^{-1}$ the amplitude, and $t_{tot} = 53 \text{ h}$ is the period of the synoptic-scale
 241 low-level forcing.

242 According to the findings of Gisinger et al. (2017), the peculiarity of IOP 9 was the southward
 243 deflection of the core of the subtropical jet stream (STJ) to about 40° S in the region of NZ (also

244 see Fig. 7b). The southward deflection of the subtropical jet is evident at 200 hPa, especially at
245 early times (Fig. 7b). Later, the 200 hPa winds decreased markedly over the SI (Figs. 7d and 7f).
246 At lower levels, a branch of the STJ separated from the main jet and diverted south (Fig. 7a). This
247 branch of the STJ passed the SI during the displayed sequence (Figs. 7a, c). On 30 June 2014
248 12 UTC, 300 hPa winds increased again with the approaching front reaching about 35 m s^{-1} over
249 the SI (Fig. 7e). This changing upper tropospheric wind conditions resulted in varying propagation
250 conditions in the UTLS region for the excited mountain waves during IOP 9.

251 Figure 8a displays vertically smoothed and temporally averaged profiles of U_{\perp} from the IFS
252 taken at the above defined upstream point in Fig. 1. A double-jet structure dominated the wind
253 profile in the UTLS during the first half of 29 June 2014 (blue solid line in Fig. 8a). The respective
254 U_{\perp} maxima of 40 m s^{-1} at $\approx 11 \text{ km}$ and of 32 m s^{-1} at $\approx 15 \text{ km}$ altitude belong to the split branch
255 of the STJ and the STJ itself (Fig. 7a, b). In between the double jet at around 13.5 km altitude, the
256 minimum wind speed of U_{\perp} was 25 m s^{-1} . As the STJ passed the SI, the upper peak of the double
257 jet reduced to 25 m s^{-1} (violet line of 14 UTC to 16 UTC average in Fig. 8a). The lower-level
258 peak broadened in altitude and became smaller in magnitude. The depth of minimum wind layer
259 between the two jets narrowed and the U_{\perp} decreased in this layer creating a shallow layer of strong
260 negative shear between 12 km and 13.5 km altitude (shaded in Fig. 8a).

261 At the end of 29 June 2014, the lower-level split-branch jet had moved downstream the SI (Fig.
262 7c) and only a weak wind maximum remained at $\approx 10 \text{ km}$ altitude (green line in Fig. 8a). At
263 this time, the edge of the STJ was located over the SI (Fig. 7d), with maximum upstream U_{\perp}
264 of $\approx 30 \text{ m s}^{-1}$ at 14 km altitude (green line in Fig. 8a). Above, a still sharp wind reduction to
265 18 m s^{-1} within an altitude range of 1.5 km is found. Later, after the passage of the cold front
266 (Fig. 5e), the wind profile became more uniform near the tropopause (Fig. 8a). The difference
267 between the wind speed in the lower and middle stratosphere decreased from 20 m s^{-1} on 29 June

268 to 10 m s^{-1} later on 30 June (Fig. 8a). At all times, the cross-mountain wind speeds increased
 269 above 30 km altitude due to the presence of the polar night jet (PNJ) over the SI.

270 At the time of occurrence of the double-jet structure, a low-stability layer with reduced values
 271 of the squared Brunt-Vaisala frequency $N^2 = g \partial \ln(\theta) / \partial z$ was located beneath the tropopause (cf.
 272 blue shaded values of $N^2 < 0.5 \cdot 10^{-4} \text{ s}^{-2}$ in Fig. 2). This results in a sharp tropopause and a
 273 pronounced tropopause inversion layer (TIL, Birner et al. 2002)) which was frequently found over
 274 NZ during DEEPWAVE Gisinger et al. (2017, Fig. 4a in). As visible in Fig. 2, the tropopause
 275 descended from about 11.5 km to about 8.5 km altitude from 08 UTC 29 June till 19 UTC 30 June.
 276 Consequently, the Scorer parameter (Scorer 1949)

$$\ell(z) = \sqrt{\frac{N^2(z)}{U_{\perp}^2(z)} - \frac{1}{U_{\perp}(z)} \frac{d^2 U_{\perp}(z)}{dz^2}} \quad (1)$$

277 shows a distinct minimum varying between 8.5 km and 6 km altitude (Fig. 8b). In linear, steady-
 278 state theory, the Scorer parameter indicates vertically propagating waves for horizontal wavenum-
 279 bers $k = 2\pi/\lambda_x < \ell$ and evanescent waves for $k > \ell$. The critical wavenumber $k_{crit} = \ell$ and the cor-
 280 responding critical horizontal wavelength $\lambda_{crit} = 2\pi/\ell$ marks the transition between both regimes.
 281 The pronounced low-stability layer below the tropopause resulted in a large $\lambda_{crit} \approx 30 \text{ km}$ during
 282 early 29 June (blue line of 08–10 UTC average in Fig. 8b). Until late 30 June 2014 increasing
 283 stabilization (Fig. 2) and decreasing wind speeds lead to a smaller $\lambda_{crit} \approx 10 \text{ km}$ in the upper
 284 troposphere (orange line in Fig. 8b).

285 The analysis of the meteorological situation around the SI revealed the low-level forcing and
 286 the propagation conditions in the UTLS region. Both will have an influence on the observed wave
 287 activity at flight level.

288 Finally, Fig. 9 illustrates the mesoscale flow by means of the vertical wind component and
 289 isentropic surfaces from the innermost domain of the WRF simulations interpolated along the

290 Mt.-Aspiring-2b transect. Four different times are selected to cover the maximum and decelerating
291 forcing phases. At all times, up- and downdrafts apparently associated with individual mountain
292 peaks dominate the vertical wind field in the troposphere. The tropopause, marked by decreasing
293 spacing of the isentropes, descended during the displayed period and the TIL weakened (cf. Figs.
294 9a and 9d). In the lower stratosphere, propagating waves of varying intensity and vertical extent
295 appear mainly over the mountain peaks and are characterized by vertical wavelengths of 5 - 6 km.
296 During the decelerating forcing phase (Fig. 9c, d) and with the weakening of the TIL (Fig. 2),
297 the amplitudes of the simulated gravity waves in the stratosphere become larger with more than
298 3 m s^{-1} (Fig. 9d). Most pronounced in Fig. 9c, isentropes become very steep in the altitude region
299 between ≈ 15 and ≈ 20 km. Near the end of IOP 9 gravity waves of even larger amplitudes having
300 horizontal wavelengths of about 20 km and large vertical wavelengths are found at the lower edge
301 of the PNJ (Fig. 9d, orange profile above 30 km in Fig. 8a)

302 4. Results

303 Aircraft observations along the Mt.-Aspiring-2b transect exist only during maximum (covered
304 by RF12) and decelerating (covered by FF01, RF13 and FF02) forcing phases. These different
305 phases are further divided into maximum forcing phases part I and II, and in early, mid and late
306 decelerating forcing phases according to the changing propagation conditions in the UTLS (see
307 Fig. 2 and Table 2). In this section, we analyze the wave response in the UTLS (Section 4a) by
308 means of vertical displacements and along-track momentum fluxes. The vertical propagation into
309 the mesosphere is investigated in Section 4b.

310 *a. Wave Response in the UTLs*

311 1) VERTICAL DISPLACEMENTS

312 Figure 10 illustrates the varying wave activity over the Mt.-Aspiring-2b-transect by means of
313 vertical displacement $\eta = \int_0^x \frac{w'(x)}{u_{track}(x)} dx_{track}$ (Smith et al. 2008) derived from the flight-level vertical
314 velocity perturbation w' and the along-track wind component u_{track} of the four research flights
315 RF12, FF01, RF13 and FF02.

316 During the maximum forcing phase, η decreases slightly from the upstream locations to the
317 middle of the main mountain ridge where a pronounced increase of about 1300 m is found (RF12,
318 Fig. 10a, see also Fig. 9a in Smith et al. 2016). Small-amplitude fluctuations of η extend down-
319 wind over the SI. Especially for leg 1 and leg 18, those fluctuations show small horizontal scales
320 of $\lambda_x \approx 10$ km downstream of the Dunstan Mountains which is located at 20 km distance. Legs 18
321 and 22 further show a region of very small-scale perturbations ($\lambda_x < 2$ km) between -100 and
322 -75 km distance over the Mt.-Aspiring massif. In Smith et al. (2016), the threshold of $\lambda_x = 2$ km
323 is used to denote turbulent motions. We follow this terminology in this study.

324 The beginning of the decelerating forcing phase was covered by the subsequent Falcon research
325 flight FF01 (Fig. 10b). It reveals vertical displacements with peak-to-peak amplitudes up to
326 1500 m extending over the main mountain ridge (around distance = -80 km). This part of the
327 η -curves is dominated by long waves with $\lambda_x \approx 200$ km. Their upstream phase tilt with height
328 (estimated phase line in black in Fig. 10b) is characteristic for upward propagating hydrostatic
329 mountain waves based on steady-state assumptions. Supporting this finding, also the mountain
330 waves in the WRF simulations show an upstream phase tilt in the w -field at about the same hor-
331 izontal distance (≈ -60 km) between 8 and 11 km altitude (Fig. 9c). In addition, shorter ($\lambda_x \approx$
332 20 - 30 km), high-amplitude (up to 1200 m) η -oscillations are found above and in the lee of the

333 Dunstan Mountains (at 20 km distance) and above the range of Mt. Pisgah (at 90 km distance, Fig.
334 10b). As mentioned above, FF01 leg 1 had slightly different track coordinates than the other legs,
335 especially, at the downstream part of the leg (thin red line in Fig. 1). Therefore, the oscillations
336 observed directly over the Dunstan Mountains could not be detected during FF01 leg 1. In agree-
337 ment with the other legs, the large-scale response with $\lambda_x \approx 200$ km is well captured. Compared
338 to RF12, small-scale wave activity with $\lambda_x \approx 10$ km is only found downstream of the SI (leg 3 and
339 leg 4).

340 During the mid and late decelerating forcing phases, the observed wave activity is strongly
341 reduced. While peak-to-peak η -amplitudes of up to 1500 m are found during RF12 and FF01,
342 they are reduced during RF13 and FF02 reaching maximum values of around 500 m (Fig. 10c,
343 d). The large-scale waves which showed up in the vertical displacements of FF01 can no longer
344 be clearly found for RF13 and FF02 (Fig. 10c, d). In addition, the small-scale η -oscillations
345 do not show a strong connection to underlying dominant topographic features towards the end of
346 IOP 9 (Fig. 10d). The interim occurrence of horizontally long waves, as well as the pronounced
347 temporal decay of the η -amplitudes in the decelerating forcing phase are the key findings of the
348 vertical displacement analyses.

349 2) MOMENTUM FLUXES

350 The transience of the wave response during IOP 9 is further quantified by means of vertical fluxes
351 of along-track momentum MF_{track} . Figure 11a displays all leg-integrated aircraft observations and
352 the respective fluxes calculated from the transient WRF simulation at typical flight altitudes of
353 8 km (upper troposphere) and 13 km (lower stratosphere). $MF_{track} < 0$ mainly indicates downward
354 transport of positive momentum, i. e. upward propagating gravity waves in the westerly flow. A

355 change of sign denotes a change of vertical propagation direction. In Fig. 11 we show $-MF_{track}$
356 and use the values without sign in the following, but we point out sign reversals when present.

357 The observed $-MF_{track}$ increases from $\approx 10 \text{ kN m}^{-1}$ to $\approx 70 \text{ kN m}^{-1}$ in the maximum forcing
358 phase (green dots of RF12 in Fig. 11a). During early decelerating forcing phase, the leg-integrated
359 fluxes spread by $\approx 110 \text{ kN m}^{-1}$ between the tropospheric (first violet dot at 130 kN m^{-1} in Fig.
360 11a) and the stratospheric (last two violet dots at $\approx 10 \text{ kN m}^{-1}$ in Fig. 11a) flight altitudes of FF01.
361 In the subsequent mid decelerating forcing phase RF13 shows stratospheric flux values between
362 ≈ 15 and $\approx 30 \text{ kN m}^{-1}$. During the final research flight FF02 $-MF_{track}$ is $< 15 \text{ kN m}^{-1}$ and even
363 reverses sign.

364 The simulated tropospheric $-MF_{track}$ (black dashed line in Fig. 11a) oscillates throughout the
365 IOP 9. Maximum values of about 200 kN m^{-1} are attained during the early decelerating forcing
366 phase. The simulated stratospheric $-MF_{track}$ (light blue dashed line in Fig. 11a) is about constant
367 at $\approx 40 \text{ kN m}^{-1}$ during maximum forcing phase part I. The maximum of $\approx 130 \text{ kN m}^{-1}$ occurs at
368 the transition from maximum forcing phase part II to early decelerating forcing phase. Thereafter,
369 stratospheric $-MF_{track}$ fluctuates like the tropospheric $-MF_{track}$, but with lower amplitudes. Gen-
370 erally, stratospheric $-MF_{track}$ -values are smaller than the tropospheric values, except a few hours
371 during maximum forcing phase part II.

372 The simulated $-MF_{track}$ -values fairly follow the observed increase of stratospheric $-MF_{track}$ -
373 values during RF12 (Fig. 11a). Simulated and observed tropospheric momentum fluxes during
374 FF01 are larger than the stratospheric ones. However, the simulated values are larger by up to
375 100 kN m^{-1} compared to the observed ones. The simulations further overestimate $-MF_{track}$ of
376 RF13 and FF02 by more than 30 kN m^{-1} . Despite the quantitative differences of simulated and
377 observed fluxes, their temporal evolutions show increasing fluxes during maximum forcing phase
378 part I, strongest fluxes at the transition from maximum forcing phase part II to early decelerating

379 forcing phase and lower values thereafter. This temporal evolution reflects a retarded maximum
380 of UTLS fluxes (6 – 14 hours) after the maximum upstream low-level forcing (see Fig. 6).

381 For linear, steady, non-dissipating mountain waves the Eliassen-Palm relation links the vertical
382 energy flux to the scalar product of horizontal wind (\mathbf{U}) and horizontal momentum flux (\mathbf{MF}):
383 $EF_z = -\mathbf{U} \cdot \mathbf{MF}$ (Eliassen and Palm 1960). Generally, both the observations (colored in Fig. 12)
384 and the WRF simulations at 13 km altitude (light blue) satisfy this linear relation. The slopes of
385 the corresponding linear regressions are near unity and offsets are relatively small. The largest
386 scatter and lowest Pearson correlation coefficient ($R^2 = 0.38$) occurs for the WRF simulation at
387 8 km altitude, indicating non-linear, unsteady processes like wave breaking and wave reflection
388 in the upper troposphere. Deviations from the linear relation mainly occurred in the troposphere
389 during the maximum forcing phase. The observations and the stratospheric WRF simulations, in
390 contrast, reveal less scatter and R^2 -values close to 1.

391 In the following, we investigate if the evolution and magnitude of $-MF_{track}$ during this transient
392 wave event can be described by $-MF_{track}$ -values from a series of 2D WRF runs initialized at 00,
393 06, 12, 18 UTC on 29 June and at 00, 06 UTC on 30 June, respectively. We selected the period
394 from 30 to 48 h lead time to average $-MF_{track}$ -values of the 2D simulations and compare these to
395 the $-MF_{track}$ -values of the transient run and the observations. In this simulation period, the flow
396 in all 2D runs reaches a quasi-steady state. Intentionally, we use the term “quasi-steady” to point
397 out that there still might be unsteady effects involved due to wave-wave and wave-mean-flow
398 interactions.

399 Figure 13 shows the leg-integrated $-MF_{track}$ -values of the quasi-steady runs at 13 km altitude as
400 a function of run time after initialization. After a spin-up time with maximum fluxes, all runs show
401 decreasing or nearly steady $-MF_{track}$ -values. Based on the temporal evolution of their $-MF_{track}$ -
402 values the six runs can be divided into two groups. The first group is initialized in the accelerating

403 and maximum forcing phases at 00, 06 and 12 UTC on 29 June. The second group is initialized in
404 the transition from maximum to decelerating forcing phases at 18 UTC on 29 June, 00, 06 UTC on
405 30 June. The $-MF_{track}$ -values of the first group rise only little and reach a quasi-steady state after
406 ≈ 10 hours run time with $15 < MF_{track} < 40 \text{ kN m}^{-1}$. In contrast, $-MF_{track}$ -values of the second
407 group increase to values $> 200 \text{ kN m}^{-1}$ for the 18 UTC 29 June and 00 UTC 30 June runs and
408 to $> 100 \text{ kN m}^{-1}$ for the 06 UTC 30 June run, respectively. After this maximum, the simulated
409 fluxes drop off to values between $1/2$ and $1/8$ of their individual maxima. Another difference to
410 the earlier runs is that the last three runs later approach their quasi-steady states after ≈ 30 h (gray
411 shaded in Fig. 13). Momentum fluxes of the runs during the decelerating forcing phase decrease
412 gradually in time.

413 Error bars with the minimum, mean and maximum $-MF_{track}$ -values of the quasi-steady runs at
414 8 and 13 km altitude were computed within 30 to 48 h after their initializations and are added in
415 Fig. 11a. The three quasi-steady runs initialized in the accelerating and maximum forcing phases
416 reproduce the observed and simulated low stratospheric fluxes, but show smaller values than the
417 transient run by 10 to 20 kN m^{-1} for the troposphere. The largest $-MF_{track}$ -values among all
418 quasi-steady runs are simulated by the 18 UTC 29 June run initialized at the end of the maximum
419 forcing phase. These values compare well with those of the fully transient run. The run initialized
420 in the early decelerating forcing phase at 00 UTC on 30 June shows lower tropospheric values
421 than the transient run for this time and than the observation of FF01 leg 2 (first violet dot in Fig.
422 11). At 13 km altitude, this run and the later run initialized at 06 UTC on 30 June have also lower
423 flux values than the transient run, but their values fit better to the stratospheric observations of
424 FF01 and RF13 compared to the transient run. Generally, the three runs of the first group show a
425 smaller spread between minima und maxima than the runs of the second group. According to this
426 comparison, the evolution of the observed $-MF_{track}$ in the lower stratosphere from the maximum

427 forcing phase to the mid decelerating forcing phase largely follows a sequence of fluxes simulated
428 by individual quasi-steady runs initialized in the same forcing phases.

429 3) MOMENTUM CARRYING WAVE SCALES

430 The amount of wave momentum carried by gravity waves depends on the horizontal wavelength
431 λ_x (Smith et al. 2016). Figures 11b - c show $-MF_{track}$ calculated for perturbations u'_{track} , w' asso-
432 ciated with large-scale ($\lambda_x > 30$ km) and small-scale ($\lambda_x \leq 30$ km) waves as reconstructed by the
433 wavelet analysis, respectively. A value of $\lambda_x = 30$ km is an appropriate cutoff wavelength for the
434 small-scale contributions as the analyzed airborne data reveal a minimum of wave momentum and
435 energy around $30 < \lambda_x < 60$ km (not shown). Therefore, wave momentum and energy contribu-
436 tions of $\lambda_x > 30$ km can be equated to those of $\lambda_x > 60$ km. The contributions of large-scale (Fig.
437 11b) and of small-scale waves (Fig. 11c) to the leg-integrated momentum flux $-MF_{track}$ evolve
438 differently in time. In the following, we discuss the individual forcing phases step by step.

439 The peaks in the total simulated tropospheric $-MF_{track}$ during the maximum forcing phase part
440 I (Fig. 11a) can be attributed to long waves with $\lambda_x > 30$ km (Fig. 11b). Afterwards, these tro-
441 pospheric flux values decrease and reach even negative values around 15 UTC. Similar to the ob-
442 served stratospheric fluxes with $\lambda_x > 30$ km the simulated fluxes increase until the transition from
443 maximum to decelerating forcing phase. However, the observed values are about 20 to 30 kN m^{-1}
444 larger than the simulated one, except for the first RF12 leg. Observed and simulated waves with
445 $\lambda_x \leq 30$ km only marginally contribute to the total flux in the UTLS (Fig. 11c) during this period.
446 In the beginning of the maximum forcing phase part II, the WRF simulation already shows in-
447 creasing small-scale wave activity, whereas the observations still give around zero flux values as
448 illustrated by the last two legs of RF12 (Fig. 11c).

449 During the transition from maximum to decelerating forcing phase both short and long waves
450 contribute to the broad peaks of the total simulated $-MF_{track}$ by about 110 kN m^{-1} for 8 km
451 altitude, respectively, and by 65 kN m^{-1} for 13 km altitude, respectively, as visible in Fig. 11b,
452 c. As in the preceding maximum forcing phase, the observations in the early decelerating forcing
453 phase exhibit higher flux values for $\lambda_x > 30 \text{ km}$ than the simulations, except for one leg (Fig. 11b).
454 For the small-scale waves, observed fluxes are about half the simulated values in the troposphere
455 (first violet dot in Fig. 11c). The observed momentum flux carried by waves with $\lambda_x \leq 30 \text{ km}$
456 even reverses sign in the stratosphere (last two violets dots in Fig. 11c) which is not found in the
457 simulation.

458 During the mid decelerating forcing phase both simulations and observations reveal a trend
459 of decreased fluxes of large-scale waves with about similar values. Apparently, the excitation
460 of long waves has ceased since the beginning of the decelerating forcing phase. Therefore, the
461 oscillating character of the total simulated $-MF_{track}$, as visible in Fig. 11a, during the mid and
462 late decelerating forcing phases results from small-scale wave activity. Obviously, the simulated
463 $-MF_{track}$ of small-scale waves is overestimated compared to the observations of RF13 and FF02
464 (Fig. 11c). Wagner et al. (2017) explain this overestimation with a lack of turbulent diffusion in
465 the WRF simulation.

466 The wavelength decomposition of $-MF_{track}$ of the quasi-steady runs reveals also intensifying
467 large-scale wave activity towards the transition from maximum to decelerating forcing phase (error
468 bars in Fig. 11b). Thereafter, decreasing flux values are simulated for $\lambda_x > 30 \text{ km}$. The evolution
469 of the stratospheric flux values of the transient run for $\lambda_x > 30 \text{ km}$ can be represented by the
470 individual quasi-steady runs, as the stratospheric $-MF_{track}$ -values of the fully transient run are
471 covered by the variability (error bars) of the quasi-steady runs. As for the fully transient run,
472 these simulated values of the 2D quasi-steady runs are mostly smaller than the observed values.

473 The range of tropospheric $-MF_{track}$ -values of the first group of quasi-steady runs is smaller than
474 $-MF_{track}$ -values of the fully transient run. The second group of quasi-steady runs, with its larger
475 spread between minima and maxima better capture the flux values of the fully transient simulation.

476 Transiently simulated and observed flux values for $\lambda_x \leq 30$ km lie within the range of the error
477 bars for the first group of the quasi-steady runs both in the troposphere and stratosphere (Fig.
478 11c). The small-scale flux values of the second group differ from the observations and the fully
479 transient simulation, except for the stratospheric values of the last quasi-steady run at 06 UTC
480 30 June. The largest difference between observed and quasi-steady fluxes appears during the early
481 decelerating forcing phase when fluxes of reversed sign for the small-scale waves are detected in
482 the stratosphere.

483 Summarizing, the long waves dominate the transient behaviour in the stratosphere. Observa-
484 tions reveal that the small-scale wave contributions have small flux values and do not vary much
485 in time. Large positive and large negative flux values of the small-scale waves occur in the tro-
486 posphere and stratosphere, respectively, during the early decelerating forcing phase. The WRF
487 simulations are able to represent the general evolution of the large-scale component, whereas the
488 small-scale contributions are overestimated.

489 4) LOCAL SCALE-DEPENDENT FLUXES

490 The previous analysis concentrated on the temporal evolution of the leg-integrated along-track
491 momentum fluxes. Next, the extended wavelet transform as described in the Appendix is applied
492 to quantify the horizontal wavelengths associated with locations of significantly enhanced (5% sig-
493 nificance level) vertical energy flux $EF_{z_n}(s_j)$ and along-track momentum flux $MF_{track_n}(s_j)$. Based
494 on the respective signs of the spectral amplitudes of $MF_{track_n}(s_j)$ and $EF_{z_n}(s_j)$ the dominant verti-

495 cal propagation direction of wave packets (from linear, steady-state theory) was determined along
496 selected GV and Falcon flight legs.

497 During the maximum forcing phase part I, the GV RF12 leg 6 (at around 12 km altitude) is dom-
498 inated by positive spectral amplitudes of $0.1 < EF_{z_n}(s_j) < 0.3 \text{ kW m}^{-1}$ at horizontal wavelengths
499 between 40 and 120 km. These values are statistically significant between $60 \text{ km} \lesssim \lambda_x \lesssim 80 \text{ km}$
500 and are located over the main ridge of the Southern Alps (Fig. 14a). The spatial coincidence of
501 the spectral peaks of negative momentum flux $-0.01 < MF_{track_n}(s_j) < -0.007 \text{ kN m}^{-1}$ (slightly
502 shifted downstream and to smaller wavelengths) with the $EF_{z_n}(s_j) > 0$ pattern suggests an upward
503 propagating gravity wave with $\lambda_x \approx 60-70 \text{ km}$ (Fig. 14b). The location and the wave scale are in
504 agreement with the dominating signal of the vertical displacements in Fig. 10a. Another significant
505 region in both cospectra with $\lambda_x \approx 10 \text{ km}$ is located over Mt. Alta at -45 km distance. In con-
506 trast to the former region, here negative spectral amplitudes of $-0.3 < EF_{z_n}(s_j) < -0.1 \text{ kW m}^{-1}$
507 coincide with positive momentum fluxes of $0.007 < MF_{track_n}(s_j) < 0.01 \text{ kN m}^{-1}$, suggesting a
508 downward propagating gravity wave.

509 In the maximum forcing phase part II, the GV detected strong turbulence along the flight leg 22
510 (altitude of 13.5 km) above the main mountain range between -100 and -80 km distance (Fig.
511 14c, d). This enhanced turbulence is reflected by significant flux values in the wavelength range
512 $400 \text{ m} \lesssim \lambda_x \lesssim 2 \text{ km}$. During the same flight leg and at approximately the same location, enhanced
513 spectral amplitudes with $0.1 < EF_{z_n}(s_j) < 0.3 \text{ kW m}^{-1}$ and $0.01 < MF_{track_n}(s_j) < 0.03 \text{ kN m}^{-1}$
514 (significant in $MF_{track_n}(s_j)$) are found at $\lambda_x \approx 30 \text{ km}$ (Fig. 14c, d). The same sign of $EF_{z_n}(s_j)$ and
515 $MF_{track_n}(s_j)$ excludes vertically propagating linear waves. The superposition of longer and shorter
516 spectral components suggests local wave breaking in the lower stratosphere at this location. During
517 the same GV flight leg 22, linear upward propagating mountain waves with $10 \text{ km} \lesssim \lambda_x \lesssim 20 \text{ km}$
518 were detected above the Dunstan Mountains at about 20 km distance with significant spectral

519 amplitudes of $0.3 < EF_{z_n}(s_j) < 0.5 \text{ kW m}^{-1}$ and $-0.03 < MF_{track_n}(s_j) < -0.01 \text{ kN m}^{-1}$ (Fig. 14c,
 520 d). This is the first detection of upward propagating gravity waves over the Dunstan mountains
 521 during the maximum forcing phase, 7 h after the begin of airborne observations.

522 During the early decelerating forcing phase, the Falcon flight FF01 observed strong, upward
 523 propagating mountain waves in leg 2 (8 h later than GV leg 22) with $EF_{z_n}(s_j) > 1 \text{ kW m}^{-1}$,
 524 $-0.05 < MF_{track_n}(s_j) < -0.03 \text{ kN m}^{-1}$ and $12 \text{ km} \lesssim \lambda_x \lesssim 35 \text{ km}$ wavelength in the upper tropo-
 525 sphere also above the Dunstan Mountains at $\approx 20 \text{ km}$ distance (Fig. 15a, b). Here, the enhanced
 526 spectral amplitudes extend about 50 km downwind from the Dunstan Mountains. Along the same
 527 flight track, about one hour later and 1 km higher than the previous flight leg 2, large negative
 528 energy flux values of $-1 < EF_{z_n}(s_j) < -0.7 \text{ kW m}^{-1}$ and large positive momentum flux values
 529 of $0.05 < MF_{track_n}(s_j) < 0.07 \text{ kN m}^{-1}$ indicate large-amplitude downward propagating gravity
 530 waves above and downstream of the Dunstan Mountains (Fig. 15c, d).

531 The mid and late decelerating forcing phases were already characterized by considerably de-
 532 creased wave amplitudes observed during RF13 and FF02 as described above for the leg-integrated
 533 fluxes (Fig. 11a) and the vertical displacements (Fig. 10c, d). At around 9 km altitude within the
 534 tropopause, positive smaller energy flux values of $0.1 < EF_{z_n}(s_j) < 0.3 \text{ kW m}^{-1}$ with $\lambda_x \approx 18 \text{ km}$
 535 and $\lambda_x \approx 30 \text{ km}$ of the FF02 leg 2 stretch between the Dunstan Mountains and the Mt. Pisgah
 536 range (Fig. 16a). The fair consistency with colocated significant negative momentum flux val-
 537 ues of $-0.007 < MF_{track_n}(s_j) < -0.003 \text{ kN m}^{-1}$ indicates weak upward propagating waves (Fig.
 538 16b). But also downward propagating waves were identified by the wavelet analysis at this stage
 539 of the transient evolution. Two negative significant energy flux patches of $-0.07 < EF_{z_n}(s_j) <$
 540 -0.03 kW m^{-1} at $\lambda_x \approx 10 \text{ km}$ exist in the lee of the SI. They appear at the same spatial location as
 541 a significant positive momentum flux signature of $0.003 < MF_{track_n}(s_j) < 0.007 \text{ kN m}^{-1}$.

542 The subsequent leg 3 of FF02 was conducted at around 10.5 km altitude above the tropopause.
 543 The Falcon observed a significant upward propagating wave of 20 - 30 km wavelength with
 544 $0.1 < EF_{z_n}(s_j) < 0.3 \text{ kW m}^{-1}$ and $-0.03 < MF_{track_n}(s_j) < -0.01 \text{ kN m}^{-1}$ directly above and
 545 downstream of the Dunstan Mountains (Fig. 16c, d). Smaller patches of downward propagat-
 546 ing waves with $-0.3 < EF_{z_n}(s_j) < -0.1 \text{ kW m}^{-1}$, $0.003 < MF_{track_n}(s_j) < 0.007 \text{ kN m}^{-1}$ and
 547 $\lambda_x \approx 12 \text{ km}$ appear at around -10 and 100 km distance. Not only over the Dunstan Mountains,
 548 but also upstream at around -60 km distance an upward propagating wave with significant pos-
 549 itive energy flux values of $0.1 < EF_{z_n}(s_j) < 0.3 \text{ kW m}^{-1}$ and significant negative momentum
 550 flux values of $-0.007 < MF_{track_n}(s_j) < -0.003 \text{ kN m}^{-1}$ can be observed over the Mt.-Aspiring
 551 massif. During this late decelerating forcing phase, small-amplitude short waves between 9 and
 552 30 km wavelength thus dominate over the Dunstan Mountains, the Mt.-Aspiring and the Mt. Pis-
 553 gah range, i. e. all outstanding peaks along the Mt.-Aspiring-2b cross-section. In contrast to the
 554 previous Falcon flight FF01, there are no remarkable differences between wave signatures at the
 555 upper-tropospheric and the lower-stratospheric flight levels.

556 Previously identified contributions of small-scale and large-scale waves (Section 3) to leg-
 557 integrated fluxes were now attributed to different mountain peaks and ranges. Upward propagating
 558 large-scale waves were detected only during the maximum forcing phase over the main mountain
 559 ridge. Small-scale waves with larger flux values dominated the decelerating forcing phase. Due
 560 to downward propagating waves, leg-integrated fluxes are small or even of reversed sign at strato-
 561 spheric levels in the decelerating forcing phase.

562 *b. Vertical Propagation into the Mesosphere*

563 As mentioned above (Section 3), the vertical wave propagation during the maximum forcing
 564 phase part I is influenced by the existence of a low-stability layer associated with the passing STJ.

565 To illustrate this effect, we show approximated, density-corrected vertical velocity perturbations w'
 566 obtained from the balloon ascent rates calculated according to Reeder et al. (1999) and Lane et al.
 567 (2000). The 11:29 UTC sounding has large peak-to-peak amplitudes up to 4 m s^{-1} in the lower
 568 and mid-troposphere (Fig. 17a). Above, in the UTLS, the amplitudes are damped to less than a
 569 quarter of their tropospheric value. The altitude of the damping coincides with the low-stability
 570 layer between $9 \lesssim z \lesssim 11 \text{ km}$ which is marked by the almost vertical potential temperature profile
 571 resulting in a frequent occurrence of layers with $-0.06 < \partial\theta/\partial z < 0.09 \text{ K km}^{-1}$ in the upper tro-
 572 posphere (black line and gray shaded layers in Fig. 17a). Also, as shown by our Fig. 2 and by Fig.
 573 4 of Gisinger et al. (2017) the strength of the TIL is enhanced in this period. An increased hydro-
 574 static reflection coefficient r up to 0.57 was documented in Fig. 5 in Gisinger et al. (2017). Linear
 575 theory predicts, that the net upward energy flux is $(1 - r^2)$ times the flux of the incident wave
 576 (Eliassen and Palm 1960). The hydrostatic reflection coefficient (Eliassen and Palm 1960) can be
 577 calculated for large Richardson number ($Ri \gg 1/4$), i. e. no or negligible vertical shear, according
 578 to $r \approx \frac{N_S - N_T}{N_T + N_S}$, where N_T and N_S are the representative mean Brunt-Vaisala frequencies of the tro-
 579 posphere and the stratosphere (Keller 1994). The low-stability layer in the upper troposphere, i. e.
 580 a small N_T , thus results in a larger r , less net upward energy flux (downward momentum flux) and
 581 damped amplitudes above. Therefore, further aloft, the w' -amplitudes remain small (Fig. 17a).

582 During the maximum forcing phase part II, w' -amplitudes are reduced within the troposphere
 583 (17:25 UTC Lauder sonde, cf. Fig. 17b) compared to the former sounding. However, the w' -
 584 amplitudes have doubled in the entire stratosphere in comparison to those during maximum forcing
 585 phase part I (11:29 UTC radiosonde, Fig. 17a). Also the vertical gradient of potential temperature
 586 has increased in the upper troposphere giving higher values of N_T (less gray shaded layers of
 587 $-0.06 < \partial\theta/\partial z < 0.09 \text{ K km}^{-1}$ in Fig. 17b). This reduces the difference between the maximum
 588 of N and its tropospheric value. In agreement with the observed increase of N_T , the simulated

589 TIL has weakened in strength (Fig. 2) and the hydrostatic reflection coefficient is reduced to
590 around 0.5 during this period (Fig. 5 in Gisinger et al. 2017). The increasing penetrability of the
591 upper troposphere coincides with the downstream advection of the low-stability layer during the
592 maximum forcing phase part II (Section 3, Fig. 8b). Furthermore, wave breaking is indicated by a
593 nearly adiabatic layer at about 14 km altitude, also gray shaded in Fig. 17b as $-0.06 < \partial\theta/\partial z <$
594 0.09 K km^{-1} , which is located in the minimum wind layer between the peaks of the double jet
595 (Fig. 8a).

596 During the early decelerating forcing phase, large-amplitude vertical velocity fluctuations of
597 on average $\pm 1.5 \text{ m s}^{-1}$ exist within the troposphere and extend up to around 19 km altitude
598 (23:33 UTC 29 June Lauder sonde, cf. Fig. 17c). Below 19 km altitude, wave amplitudes de-
599 crease slightly with altitude attaining mean peak-to-peak amplitudes of around 3 m s^{-1} . Above,
600 peak-to-peak wave amplitudes are more strongly attenuated to around 1 m s^{-1} . The horizontal
601 projection technique of Lane et al. (2000) was applied to determine the horizontal and vertical
602 wavelengths of the large-amplitude signal of the 23:33 UTC 29 June sounding: This reveals a
603 horizontal wavelength of around 10 km with a vertical wavelength varying around 4 - 8 km in the
604 stratosphere.

605 Another remarkable finding of the radiosounding at 23:33 UTC on 29 June 2014 is the distinct
606 staircase structure of the potential temperature profile in the stratosphere (Fig. 17c). The staircase
607 structure is further quantified by detecting several stratospheric layers where $-0.06 < \partial\theta/\partial z <$
608 0.09 K km^{-1} (gray shaded in Fig. 17c) that were not present during the former soundings. Such a
609 profile with frequent occurrence of $\partial\theta/\partial z \approx 0$ in the stratosphere indicates a sequence of vertically
610 stacked mixing layers.

611 In the sounding launched during the late decelerating forcing phase (20:35 UTC 30 June Lauder
612 sonde), the vertical velocity fluctuations show locally strong wave excitation at the ground, but

613 decreasing amplitudes around the tropopause (Fig. 17d). Further aloft, w' is recorded with regular
614 fluctuations and with on average larger amplitudes of $\pm 0.5 \text{ m s}^{-1}$ than below. In comparison to
615 the former 23:33 UTC 29 June sounding, still a staircase behaviour of the potential temperature
616 profile is observed, especially between 20 and 27 km altitude, but $\partial\theta/\partial z$ has generally increased
617 and no gray shaded layers exist above 12 km altitude in Fig. 17d.

618 These soundings during the different forcing phases illustrated especially the effects of the
619 changing propagation conditions. The soundings could prove the strong damping character of
620 the low-stability layer in the upper troposphere (Fig. 17a) and could identify the minimum wind
621 layer between the peaks of the double jet as a mixing region (Fig. 17b). Stratospheric wave activity
622 increased from the maximum forcing phase to early decelerating forcing phase. During the latter
623 phase wave breaking layers were found in the stratosphere between about 15 and 25 km altitude
624 (Fig. 17c). Thereafter, stratospheric wave activity decreased (Fig. 17d).

625 As was indicated by the 23:33 UTC 29 June radiosounding, attenuated gravity waves existed
626 above the gravity wave breaking layers from $\approx 15 \text{ km}$ to $\approx 24 \text{ km}$ altitude during the early decel-
627 erating forcing phase. Hence, the question arises, if orographic gravity wave activity is observed
628 even further aloft. A measure of stratospheric and mesospheric gravity wave activity is given by
629 the gravity wave potential energy density (GWPED), calculated from temperature fluctuations of
630 the Rayleigh lidar measurements from Lauder (Fig. 18). Nine hours of measurements during 30
631 June 2014 show a transient behaviour. Especially, the mesospheric gravity wave activity reached
632 peak values of GWPED of around 110 J kg^{-1} between 15 and 16 UTC in the decelerating forcing
633 phase. The stratospheric gravity wave activity is continually decreasing from a GWPED maximum
634 of about 30 J kg^{-1} at around 11:30 UTC down to 5 J kg^{-1} at around 19:30 UTC. The stratospheric
635 and mesospheric maxima, with a plateau of wave activity in the stratopause inbetween, are time
636 shifted by around 4 hours. Assuming an upward propagation of hydrostatic mountain waves, the

637 propagation time $t_p = \frac{z}{c_{gz}}$ with $c_{gz} = \frac{\langle U_h \rangle_z^2 k}{\langle N \rangle_z}$ (see Gill 1982; Dörnbrack et al. 2011) can be estimated
638 to around 12 h up to the mesosphere with $\lambda_x \approx 200$ km, $\langle N \rangle_z \approx 0.02$ s⁻¹, $\langle U_h \rangle_z \approx 30$ m s⁻¹, where
639 $\langle \rangle_z$ denotes an average over the vertical range with $z = 60$ km from the UTLS to the mesosphere.
640 Counting back from the maximum mesospheric GWPED at 15 UTC 30 June, the resulting time is
641 close to the maximum of long wave activity in the early decelerating forcing phase (Fig. 10b and
642 11b).

643 Airborne AMTM observations obtained during the two GV research flights RF12 and RF13 on
644 29 and 30 June, respectively, confirm the delayed appearance of those long mountain waves in
645 the mesosphere: While the observations of RF12 during the maximum forcing phase show no
646 clear large-scale structures above the SI (≈ 11 UTC 29 June, Fig. 19a), the airglow observations
647 of RF13 reveal elongated maxima of the airglow brightness temperatures parallel to the main
648 mountain ridge and a minimum directly above the SI (≈ 14 UTC 30 June, Fig. 19b). The estimated
649 horizontal wavelength amounts to about 200 km and agrees with λ_x estimated from the vertical
650 displacements in the UTLS during the early decelerating forcing phase (Fig. 10b). Counting back
651 with a calculated propagation time of 15 h from 12 to 87 km altitude matches the time of maximum
652 long-wave response in the UTLS (Fig. 10b and 11b). Temperature perturbations and vertical
653 displacements have the same wavenumber dependency in the Fourier space (Smith and Kruse
654 2017) and are thus comparable in their wave spectrum. It must be noted that the large-scale wave
655 in AMTM appeared only during the last legs of RF13. Summarizing, the deep upward propagation
656 of long hydrostatic mountain waves with $\lambda_x \approx 200$ km which were observed in the UTLS during
657 the early decelerating forcing phase, up to the mesosphere, is identified by combining airborne
658 data from flight-level and the middle atmosphere.

659 5. Comparison with previous Studies and Discussion

660 In this section we discuss our results in the context of numerical studies of transiently forced
661 mountain waves, as well as in the context of previous investigations of MAP, T-REX and DEEP-
662 WAVE studies.

663 A detailed and quantitative comparison of our findings for this complex transient wave event
664 with existing theoretical and idealized numerical simulation studies (Lott and Teitelbaum 1993a,b;
665 Chen et al. 2005, 2007) is hardly possible. The analyzed wave event is not only influenced by
666 transient tropospheric forcing but also by changing propagation conditions in the UTLS region.
667 Previous studies focused on mountain waves generated during only transient tropospheric forcing
668 (Lott and Teitelbaum 1993a,b; Chen et al. 2005, 2007). In these studies, forcing and propagation
669 conditions varied temporarily at all altitudes in the same way. In contrast, our case study reveals the
670 importance of the varying propagation conditions. They include the passing upper-tropospheric
671 low-stability layer with a correspondingly strong TIL, the double peak structure of the STJ, and the
672 wave breaking in the UTLS and in the stratospheric wind minimum. Nevertheless, the observed
673 temporal dependence of the low-level cross-mountain flow with an approximated \cos^2 -variation
674 over about 53 hours and a total increase of cross-mountain wind of $\approx 20 \text{ m s}^{-1}$ corresponds to
675 values used in those theoretical and numerical studies.

676 The low-stability layer in the upper troposphere (Fig. 2) occurred in the maximum forcing phase
677 part I and resulted in decreasing values of the Scorer parameter ℓ and large λ_{crit} -values of about
678 30 km (Fig. 8b). As a result, the strength of the TIL and the reflection coefficient r for hydrostatic
679 gravity waves increased. In effect, the stratospheric wave amplitudes were strongly attenuated as
680 documented by the radiosonde observation (Fig. 17a) and the simulated vertical wind (Fig. 9a).
681 The numerical results reveal that longer waves with $\lambda_x \approx 60 \text{ km}$ were damped, too: A pair of strong

682 down- and updrafts in the lee of the main mountain ridge between -90 km and -40 km distance
683 is effectively attenuated in the upper troposphere (Fig. 9a). These findings are confirmed by the
684 small simulated and observed stratospheric momentum fluxes in the maximum forcing phase part
685 II for $\lambda_x > 30$ km in Fig. 11b.

686 Another peculiarity of the time-varying propagation conditions in the UTLS is the wave breaking
687 between the double peaks of the STJ. There, the cross-mountain wind was reduced by 15 m s^{-1}
688 over less than 2 km altitude (second shaded area in Fig. 8a, 17b). Radiosonde observations
689 revealed a mixing layer in this minimum wind layer (Fig. 17b). As the GV flew within this
690 layer, the observed nonlinearity and turbulence at flight level (Fig. 14c, d) suggests mountain
691 wave breaking. Due to this wave breaking, the observed leg-integrated momentum fluxes for
692 $\lambda_x \leq 30$ km remain negligible (Fig. 11c). This double-jet-induced wave breaking has not been
693 observed previously. However, the occurrence of gravity wave breaking in a layer of negative shear
694 above a tropopause jet was already reported by Doyle et al. (2011) and Smith et al. (2016) during
695 T-REX and other IOPs of the DEEPWAVE campaign.

696 Vertically stacked mixing layers observed in the stratospheric wind minimum by the radiosound-
697 ing during the early decelerating forcing phase (Fig. 17c) coincide with simulated wave breaking.
698 The simulated wave breaking and the resulting mixing is indicated by steep isentropes at around
699 17 km altitude (Fig. 9c). Interestingly, downward propagating waves in the lower stratosphere
700 were detected in the flight-level data during this period (Fig. 15c, d). The similarity of the hori-
701 zontal wavelength band and the same location of upward (leg 2, Fig. 15a, b) and downward (leg 4,
702 Fig. 15c, d) propagating signals suggest that the observed downward propagating wave results
703 from partial wave reflection by the breaking region located above the flight leg. Observations of
704 downward propagating waves extend further into the late decelerating forcing phase (Fig. 16). The
705 numerical simulations support the assumption of reflected mountain waves also in this phase, as

706 a gravity wave breaking region is present in the stratospheric wind minimum near 19 km altitude
707 (Fig. 9d). Upward and downward propagating waves influence the wave response at the subjacent
708 stratospheric flight levels in such a way that the observed leg-integrated momentum fluxes become
709 negligible (Fig. 11). The observational and numerical evidence of the existence of a stratospheric
710 gravity wave breaking layer confirms the findings of the so-called “valve” layer within the strato-
711 spheric wind minimum (Kruse et al. 2016). This “valve” layer attenuates upward propagating
712 waves when wave breaking occurs. Indeed, attenuated waves were observed above, indicating a
713 leakage of wave energy into the upper stratosphere during IOP 9 (Fig. 9c, 17c). In general, the
714 existence of the stratospheric wind minimum is not related to the transient mountain wave event
715 but to the location of NZ and the seasonal shift of the PNJ (Fritts et al. 2016). The “valve” layer as
716 a breaking layer depends on the amplitudes of waves that are able to propagate beyond the UTLS
717 in comparison to the magnitude of the stratospheric wind (Kruse et al. 2016). As wave amplitudes
718 in the lower stratosphere are largest during the early decelerating forcing phase, wave breaking in
719 the stratospheric “valve” layer was mainly limited to this phase. Therefore, the appearance of the
720 “valve” is also transient.

721 Kruse and Smith (2015) classified observed mountain wave cases of the DEEPWAVE cam-
722 paign into shallow and deep events depending on the reduction of horizontal stratospheric wind
723 by 20 m s^{-1} or 10 m s^{-1} , respectively, from a lower-stratospheric value of 30 m s^{-1} . Based on
724 this classification, the reduction of U_{\perp} ($\approx U_{hor}$ at this time and altitude region) from 30 m s^{-1} at
725 14 km altitude to 16 m s^{-1} at 17 km altitude (green line in Fig. 8a) places our event inbetween the
726 characteristic values of shallow and deep gravity wave propagation. Essentially, both wave atten-
727 uation and leakage of wave energy into the upper atmosphere characterize the conditions during
728 IOP 9.

729 In the UTLS, vertically propagating mountain waves achieved along-track momentum flux (ver-
730 tical energy flux) values varying from about zero up to $\approx 130 \text{ kN m}^{-1}$ ($\approx 4000 \text{ kW m}^{-1}$). Smith
731 et al. (2016) classified all DEEPWAVE IOPs into weak and strong flux events applying a thresh-
732 old value of $EF_z = 4 \text{ W m}^{-2}$ (leg-average converted to leg-integrated: $EF_z \approx 1600 \text{ kW m}^{-1}$). As
733 before, the transient character of the low-level forcing conditions and the wave attenuation does
734 not allow a unique assignment of IOP 9 to one of these classes.

735 The flow across the rugged terrain of the Southern Alps excites a broad spectrum of gravity
736 waves. During IOP 9, horizontally long waves of $\lambda_x \approx 200 \text{ km}$ were only observed during the
737 early decelerating forcing phase (Fig. 10b), when still strong cross-mountain winds passed over the
738 whole SI of NZ. The observed retarded appearance of these waves in the mesosphere (Fig. 14 and
739 Fig. 19) confirms their essentially hydrostatic character and agrees with previous studies (Smith
740 et al. 2009; Bramberger et al. 2017). Shorter waves were present in the UTLS at all times (Fig.
741 10a - d, Fig. 14 - 16). Their transient character could be observed over the Dunstan Mountains, an
742 isolated, single ridge that is by far the highest elevation seen by the incoming flow from northwest
743 in the vicinity of more than 40 km distance (Fig. 3). The role of the Dunstan Mountains can be
744 compared with the Monte Rosa case of MAP on 8 November 1999. There, only the flow over the
745 last and the highest peaks in the sequence of several ridges excited mountain waves as the air was
746 trapped in valleys located upstream (Smith et al. 2007). Therefore, findings were mainly based
747 on the observation of waves over Monte Rosa. During IOP 9, waves over the Dunstan Mountains
748 were first not observed at the stratospheric flight level (Fig. 14a, b). Only late during the maximum
749 forcing phase part II, waves over the Dunstan Mountains were detected in the lower stratosphere
750 (Fig. 14c, d), confirming improved upper-tropospheric propagation conditions for the small-scale
751 waves. Later, upward propagation in the upper troposphere (Fig. 15a, b) and partial wave reflection
752 in the lower stratosphere (Fig. 15c, d) in the early decelerating forcing phase were observed. Those

753 upward and downward propagating waves over the Dunstan Mountains dominated the small-scale
754 energy and momentum fluxes. Finally, we found the significant reduction of wave activity on the
755 basis of decreasing vertical displacements (Fig. 10b - d) and decreasing momentum and energy
756 fluxes (Fig. 15 - 16) over the Dunstan Mountains during the entire decelerating forcing phase.

757 The comparison of the 2D quasi-steady runs with the transient WRF run and the observations
758 was focused on the UTLS along-track momentum fluxes. To a large extent, the quasi-steady
759 momentum fluxes in the UTLS agree quantitatively with the transiently simulated and observed
760 values. Agreement was found for the maximum and the mid decelerating forcing phase, when
761 the variability of the steady-runs is considered (error bars in Fig. 11). The steady-state runs
762 do not capture the retarded enhancement of momentum fluxes extending further into the early
763 decelerating forcing phase in the observation of FF01 leg 2 and in the transient run. This finding
764 encourages the hypothesis that UTLS momentum fluxes as observed along the Mt.-Aspiring-2b
765 transect seem to be reproducible by individual quasi-steady 2D runs except for the retarded flux
766 enhancement during the early decelerating forcing phase. However, this statement is only based on
767 leg-integrated momentum fluxes. We did not investigate particular wave structures in the transient
768 and the stationary runs as done by Menchaca and Durran (2017) for simulations of a crossing
769 cyclone over an isolated ridge.

770 **6. Conclusions**

771 The DEEPWAVE case study presented here combines in-situ and remote-sensing measurements
772 to follow the deep vertical propagation of mountain waves from the troposphere to the meso-
773 sphere. The observational findings of a mountain wave event under transient tropospheric forcing
774 were complemented by numerical simulations covering the atmosphere up to about 33 km altitude.
775 Among a series of transient mountain wave events during DEEPWAVE, the analyzed IOP 9 was

776 the only transient case of the campaign, that was observed in such detail and duration, especially,
777 by the successive deployment of the two research aircraft NSF/NCAR GV and the DLR Falcon. In
778 this way, our study extends previous theoretical and numerical considerations of transient moun-
779 tain wave events of Lott and Teitelbaum (1993a,b) and Chen et al. (2005, 2007).

780 Although the observed low-level forcing roughly follows the sinusoidal temporal dependence
781 of the cross-mountain wind used in these studies, our case study reveals the importance of the
782 time-varying propagation conditions during the period when a migrating trough and connected
783 fronts controlled the transient forcing over NZ. With the evolving synoptic situation, the upper-
784 tropospheric stability, the wind profile as well as the tropopause strength and altitude changed,
785 and controlled the transience of the event together with the low-level forcing. Especially, the
786 occurrence of the low-stability layer and the double jet resulted in wave attenuation and mountain
787 wave breaking in the UTLS. In contrast, upper stratospheric conditions changed only marginally
788 due to the presence of a nearly steady PNJ.

789 During the event, maximum vertical displacements $\eta \approx 1500$ m and along-track momentum
790 fluxes $-MF_{track}$ varying from around zero to ≈ 130 kN m⁻¹ were observed in the UTLS. Both
791 large- and small-scale waves contributed to these maxima during the transition from maximum to
792 decelerating forcing. These maxima in the UTLS appeared with a phase shift of ≈ 8 h compared
793 to the maximum in the \cos^2 -shaped low-level cross-mountain flow.

794 Small-scale waves ($\lambda_x \leq 30$ km) appeared continuously over individual orographic peaks and
795 with large amplitudes in the troposphere. However, during the maximum forcing phase part I,
796 their vertical propagation was limited to the troposphere due to the mentioned upper-tropospheric
797 low-stability layer. The existence of a strong TIL suggests wave reflection and a reduction of net
798 upward energy flux. Therefore, simulated and observed along-track momentum fluxes of small-
799 scale waves remained small at the stratospheric flight level ($MF_{track} < 20$ kN m⁻¹). Later, when the

800 TIL weakened, λ_{crit} decreased and small-scale wave activity increased in the lower stratosphere.
801 There, however, a double jet associated with two, vertically stacked branches of the STJ stimulated
802 non-linear processes such as wave breaking.

803 Other wave breaking layers were observed between 15 and 25 km altitude inside the strato-
804 spheric wind minimum. As indicated by Kruse et al. (2016), the ratio of amplitudes of wave-
805 induced velocity perturbation to the magnitude of stratospheric wind controls if wave breaking
806 occurs. We further found that in the case of wave breaking in the stratospheric wind minimum,
807 upward propagating small-scale waves seem to be reflected at this layer, explaining the observed
808 downward propagating waves above the tropopause.

809 In accordance with the decreasing low-level wind in the decelerating forcing phase, the observed
810 short-wave along-track momentum fluxes in the UTLS diminished and achieved nearly the same
811 small values as during the maximum forcing phase. Corresponding simulated values were higher.
812 Wagner et al. (2017) explain this overestimation of the numerical simulations by a lack of turbulent
813 diffusion that comes into effect when the propagation conditions also allow for the shortest waves
814 to propagate upward.

815 The temporal appearance and intensity of horizontally longer waves differs from the small-
816 scale waves during this event. The spectral analysis revealed that long waves ($\lambda_x > 30$ km) were
817 detected only temporarily under and after the maximum in the low-level forcing. This means only
818 the strong flow over the entire island favored their excitation. In this way, the excitation of long
819 waves differs to the continuously excited small-scale waves. During the maximum forcing phase,
820 long waves carried most energy and momentum into the lower stratosphere. At the transition from
821 maximum to decelerating forcing phase, long waves with $\lambda_x > 100$ km still produce higher flux
822 values of $\approx 80 \text{ kN m}^{-1}$ compared to the small-scale waves. In contrast to the small-scale waves,
823 the change of background wind and stability does not influence the vertical propagation of long

824 waves with $\lambda_x \approx 200$ km. These waves propagated deeply upward and carried high flux values.
825 Their longer propagation time of $\mathcal{O} \approx 12$ h...15 h calculated from the UTLS region resulted in
826 a delayed appearance in the mesosphere. In total, the transience of increasing and decreasing
827 mesospheric wave activity is time-shifted to the low-level forcing by about one day.

828 Moreover, the question was investigated whether the wave response in the UTLS can be de-
829 scribed by a sequence of individual steady states. For this purpose, along-track momentum flux
830 values were simulated by six 2D WRF runs initialized at different times in the course of the event.
831 As a result, UTLS momentum fluxes seem to be reproducible by individual quasi-steady 2D runs
832 except for the flux enhancement during the early decelerating forcing phase. The well-satisfied
833 Eliassen-Palm relation for the flight level observations further suggests a quasi-steady state be-
834 haviour of the nearly linear mountain waves in the UTLS (Smith et al. 2008, 2016). Indeed, parts
835 of the wave event can be described by individual steady-states. On the other hand, our results also
836 reveal the importance of including the total transience of the event. The effect of temporally shifted
837 wave activity in the mesosphere compared to the UTLS due to dispersive wave propagation cannot
838 be captured by quasi-steady simulations. This higher altitude effect, including the excitation and
839 modified propagation of various wave scales can be considered to be another major extension to
840 existing idealized and numerical studies of transient mountain wave events.

841 *Acknowledgments.* Part of this research was funded by the German research initiative “Role of
842 the Middle Atmosphere in Climate (ROMIC)” funded by the German Ministry of Research and
843 Education in the project “Investigation of the life cycle of gravity waves (GW-LCYCLE)” and by
844 the Deutsche Forschungsgemeinschaft (DFG) via the Project MS-GWaves (GW-TP/DO1020/9-1,
845 PACOG/RA1400/6-1). Mesoscale simulations were performed at the Leibniz Institute for At-
846 mospheric Physics (IAP) in Kühlungsborn, Germany. The special project ”HALO Mission Sup-

847 port System” allowed the access to the ECMWF data. Gulfstream V (GV) data was provided by
 848 NCAR/EOL under sponsorship of the National Science Foundation. [http://data.eol.ucar.](http://data.eol.ucar.edu/)
 849 [edu/](http://data.eol.ucar.edu/). The development of the GV AMTM was funded by the NSF grant AGS-1061892, and its
 850 operations during the DEEPWAVE campaign by the NSF grant AGS-1338666. We further thank
 851 the DLR facility Flight Experiments for providing the Falcon noseboom data.

852 APPENDIX

853 Wavelet Analysis

854 The definition of the wavelet cospectra for the vertical energy and horizontal momentum flux
 855 follows Woods and Smith (2010a,b):

$$\widetilde{EF}_{z_n}(s_j) = \Re\{\widetilde{W}[p']_n(s_j)\widetilde{W}^*[w']_n(s_j)\}, \quad (\text{A1})$$

856 and

$$\widetilde{MF}_{track_n}(s_j) = \Re\{\widetilde{W}[u'_{track}]_n(s_j)\widetilde{W}^*[w']_n(s_j)\}, \quad (\text{A2})$$

857 where \widetilde{W} is the wavelet transform of the respective quantity (u'_{track} , w' and p'), \Re is the real part and
 858 the star denotes the complex conjugate. n and j are the indices in distance and scale s , respectively.
 859 According to Liu et al. (2007), the wavelet transforms are divided by the scale parameter $s^{1/2}$, i. e.
 860 they are scaled, to ensure comparable spectral peaks across scales. Apart from the definition by
 861 Woods and Smith (2010a,b), the cospectrum is further reconstructed to yield applicable physical
 862 units (factor of $\delta j \delta x^2 / C_\delta$) and to be directly comparable to the leg-integrated flux values. The
 863 spatially and spectrally integrated values of the reconstructed cospectrum thus result in the leg-
 864 integrated flux. The scaled and reconstructed cospectra are finally given by

$$EF_{z_n}(s_j) = \delta j \delta x^2 / C_\delta \cdot \widetilde{EF}_{z_n}(s_j) / s_j, \quad (\text{A3})$$

865 and

$$MF_{track_n}(s_j) = \bar{\rho} \cdot \delta j \delta x^2 / C_\delta \cdot \widetilde{MF}_{track_n}(s_j) / s_j, \quad (\text{A4})$$

866 with the unique reconstruction factor for the Morlet mother wavelet $C_\delta = 0.776$, the horizontal
 867 spacing δx and the wavenumber resolution δj (Torrence and Compo 1998; Woods and Smith
 868 2010b).

869 To differentiate gravity waves from background noise, tests for statistical significance are applied
 870 that are based on the statistical distribution of the cospectrum. Tests are conducted at the $\alpha = 5\%$
 871 significance level. What appears as significant according to the tests depends on the assumed
 872 background spectrum. First, the distribution of the cospectrum has to be determined: Assuming
 873 stochastically independent (p' and u' are not a function of w')² and normal distributed ($\mathcal{N}(\mu, \sigma)$)
 874 time series, the wavelet transforms $\widetilde{W}[w']_n(s_j)$, $\widetilde{W}[p']_n(s_j)$ and $\widetilde{W}[u']_n(s_j)$ are normal distributed,
 875 as well. This is due to the facts that the wavelet transform is a convolution of the time series with
 876 a scaled and translated wavelet function (Torrence and Compo 1998) and the statistical normal
 877 distribution is invariant with respect to a convolution. The cospectrum in turn is the real part
 878 of the product of the normal distributed wavelet transforms (Eq. A1 and A2). According to the
 879 definition of the χ^2 distribution in Ross (2009) the cospectra are then χ^2_2 distributed with 2 degrees
 880 of freedom. With the knowledge of the distribution of the cospectra, the significant parts of, e. g.,
 881 the energy flux cospectrum are thus calculated by

$$\frac{|\widetilde{EF}_{zn}(s_j)| \cdot 2}{\sqrt{|\sigma_p^2 P_k^p \cdot \sigma_w^2 P_k^w|} \cdot Q_{\chi^2_2}(1 - \alpha)} \geq 1, \quad (\text{A5})$$

882 with the original wavelet cospectrum $\widetilde{EF}_{zn}(s_j)$ of Eq. A1, the $(1 - \alpha)$ -quantile (cutoff value)
 883 $Q_{\chi^2_2}(1 - \alpha)$ of the χ^2_2 distribution, the variance σ^2 and the normalized background spectrum P_k
 884 for each quantity. To reflect the energy distribution among the wave scales, the Markov red noise

²However, it has to be noted that p' is a function of u' . See Queney (1948): $w' = U \partial \eta / \partial x$, $u' = U \partial \eta / \partial z$, $p' = -\rho U u'$.

885 spectrum was chosen as the background spectrum:

$$P_k = \frac{1 - lag1^2}{1 - 2 \cdot lag1 \cdot \cos\left(\frac{dt}{s_j \cdot FourierFactor}\right) + lag1^2}. \quad (A6)$$

886 Here, $lag1$ is an appropriately chosen lag1-autocorrelation factor of the respective time series
887 (Torrence and Compo 1998). This means, the original time series is correlated with a delayed copy
888 of itself. With a time lag of one (five) the copy would be delayed by one (five) time step(s), given by
889 the temporal resolution of the time series (here 1 s). A combination of a lag-1-autocorrelation with
890 a higher lag-5-autocorrelation $((lag1 + \sqrt{lag5})/2)$ is taken for an expected gravity wave spectrum
891 ranging from the turbulent scale up to a few hundreds of km wavelength in order. This is done to
892 include signals of large wavelengths (significant for higher time lags) and not to stress the signals
893 of the smaller wavelengths (significant for smaller time lags). Equation A5 for the calculation of
894 significant parts of the cospectra is different from Eq. 9 in Woods and Smith (2010b), especially
895 in the fact, that the latter would only expect positive $\widetilde{EF}_{zn}(s_j)$.

896 References

- 897 Birner, T., A. Dörnbrack, and U. Schumann, 2002: How sharp is the tropopause at midlatitudes?
898 *Geophys. Res. Lett.*, **29**, 45–1–45–4, doi:10.1029/2002GL015142, URL <http://dx.doi.org/10.1029/2002GL015142>.
899
- 900 Bossert, K., and Coauthors, 2015: Momentum flux estimates accompanying multiscale gravity
901 waves over Mount Cook, New Zealand, on 13 July 2014 during the DEEPWAVE campaign. *J.*
902 *Geophys. Res.*, **120**, 9323–9337, doi:10.1002/2015JD023197, URL [http://dx.doi.org/10.1002/](http://dx.doi.org/10.1002/2015JD023197)
903 [2015JD023197](http://dx.doi.org/10.1002/2015JD023197).
- 904 Bramberger, M., and Coauthors, 2017: Does strong tropospheric forcing cause large-amplitude
905 mesospheric gravity waves? A DEEPWAVE case study. *J. Geophys. Res.*, doi:10.1002/

906 2017JD027371, URL <http://dx.doi.org/10.1002/2017JD027371>.

907 Chen, C.-C., D. R. Durran, and G. J. Hakim, 2005: Mountain-wave momentum flux in an evolving
908 synoptic-scale flow. *J. Atmos. Sci.*, **62**, 3213–3231, doi:10.1175/JAS3543.1, URL <http://dx.doi.org/10.1175/JAS3543.1>.
909

910 Chen, C.-C., G. J. Hakim, and D. R. Durran, 2007: Transient mountain waves and their interaction
911 with large scales. *J. Atmos. Sci.*, **64**, 2378–2400, doi:10.1175/JAS3972.1, URL <http://dx.doi.org/10.1175/JAS3972.1>.
912

913 Dörnbrack, A., M. Leutbecher, R. Kivi, and E. Kyrö, 2011: Mountain-wave-induced record low
914 stratospheric temperatures above northern Scandinavia. *Tellus A*, **51**, 951–963, URL <http://www.tellusa.net/index.php/tellusa/article/view/14504>.
915

916 Doyle, J. D., Q. Jiang, R. B. Smith, and V. Grubišić, 2011: Three-dimensional characteris-
917 tics of stratospheric mountain waves during T-REX. *Mon. Wea. Rev.*, **139**, 3–23, doi:10.1175/
918 2010MWR3466.1, URL <http://dx.doi.org/10.1175/2010MWR3466.1>.

919 Eckermann, S. D., and Coauthors, 2016: Dynamics of orographic gravity waves observed in the
920 mesosphere over the Auckland Islands during the deep propagating gravity wave experiment
921 (DEEPWAVE). *J. Atmos. Sci.*, **73**, 3855–3876, doi:10.1175/JAS-D-16-0059.1, URL <http://dx.doi.org/10.1175/JAS-D-16-0059.1>.
922

923 Ehard, B., P. Achtert, A. Dörnbrack, S. Gisinger, J. Gumbel, M. Khaplanov, M. Rapp, and J. Wag-
924 ner, 2016: Combination of lidar and model data for studying deep gravity wave propaga-
925 tion. *Mon. Wea. Rev.*, **144**, 77–98, doi:10.1175/MWR-D-14-00405.1, URL <http://dx.doi.org/10.1175/MWR-D-14-00405.1>.
926

927 Ehard, B., B. Kaifler, N. Kaifler, and M. Rapp, 2015: Evaluation of methods for gravity wave
928 extraction from middle atmospheric lidar temperature measurements. *Atmos. Meas. Tech.*, **8**,
929 9045–9074, doi:10.5194/amtd-8-9045-2015, URL [http://www.atmos-meas-tech-discuss.net/8/
930 9045/2015/](http://www.atmos-meas-tech-discuss.net/8/9045/2015/).

931 Eliassen, A., and E. Palm, 1960: On the transfer of energy in stationary mountain waves. *Geofys.*
932 *Publ.*, **22**, 1–23.

933 Fritts, D. C., and Coauthors, 2016: The deep propagating gravity wave experiment (DEEPWAVE):
934 An airborne and ground-based exploration of gravity wave propagation and effects from their
935 sources throughout the lower and middle atmosphere. *Bull. Amer. Meteor. Soc.*, **97**, 425–
936 453, doi:10.1175/BAMS-D-14-00269.1, URL <http://dx.doi.org/10.1175/BAMS-D-14-00269.1>,
937 <http://dx.doi.org/10.1175/BAMS-D-14-00269.1>.

938 Giez, A., C. Mallaun, M. Zöger, A. Dörnbrack, and U. Schumann, 2017: Static pressure from
939 aircraft trailing-cone measurements and numerical weather-prediction analysis. *J. Aircraft*, URL
940 <http://elib.dlr.de/111325/>.

941 Gill, A. E., 1982: *Atmosphere-Ocean*. 1st ed., Academic Press, 662 pp.

942 Gisinger, S., and Coauthors, 2017: Atmospheric conditions during the Deep Propagating Gravity
943 Wave Experiment (DEEPWAVE). *Mon. Wea. Rev.*, **in print**, doi:10.1175/MWR-D-16-0435.1,
944 URL <https://doi.org/10.1175/MWR-D-16-0435.1>, <https://doi.org/10.1175/MWR-D-16-0435.1>.

945 Grubišić, V., and Coauthors, 2008: The terrain-induced rotor experiment. *Bull. Amer. Me-*
946 *eteor. Soc.*, **89**, 1513–1533, doi:10.1175/2008BAMS2487.1, URL [http://dx.doi.org/10.1175/
947 2008BAMS2487.1](http://dx.doi.org/10.1175/2008BAMS2487.1).

948 Hills, M. O. G., and D. R. Durran, 2012: Nonstationary trapped lee waves generated by the passage
949 of an isolated jet. *J. Atmos. Sci.*, **69**, 3040–3059, doi:10.1175/JAS-D-12-047.1, URL [http://dx.
doi.org/10.1175/JAS-D-12-047.1](http://dx.
950 doi.org/10.1175/JAS-D-12-047.1).

951 Jablonowski, C., and D. L. Williamson, 2011: *The Pros and Cons of Diffusion, Filters and Fixers*
952 *in Atmospheric General Circulation Models*, 381–493. Springer, Berlin, Heidelberg, doi:10.
953 1007/978-3-642-11640-7_13, URL https://doi.org/10.1007/978-3-642-11640-7_13.

954 Kaifler, B., N. Kaifler, B. Ehard, A. Dörnbrack, M. Rapp, and D. C. Fritts, 2015: Influences of
955 source conditions on mountain wave penetration into the stratosphere and mesosphere. *Geo-
956 phys. Res. Lett.*, **42**, 9488–9494, doi:10.1002/2015GL066465, URL [http://dx.doi.org/10.1002/
2015GL066465](http://dx.doi.org/10.1002/
957 2015GL066465).

958 Keller, T. L., 1994: Implications of the hydrostatic assumption on atmospheric gravity waves. *J.*
959 *Atmos. Sci.*, **51**, 1915–1929.

960 Kim, Y.-J., S. D. Eckermann, and H.-. Chun, 2003: An overview of the past, present and future
961 of gravity wave drag parametrization for numerical climate and weather prediction models.
962 *Atmos. Ocean*, **41**, 65–98, doi:10.3137/ao.410105, URL <http://dx.doi.org/10.3137/ao.410105>,
963 <http://dx.doi.org/10.3137/ao.410105>.

964 Klemp, J. B., J. Dudhia, and A. D. Hassiotis, 2008: An upper gravity-wave absorbing layer for
965 NWP applications. *Mon. Wea. Rev.*, **136**, 3987–4004, doi:10.1175/2008MWR2596.1, URL [http://
dx.doi.org/10.1175/2008MWR2596.1](http://
966 dx.doi.org/10.1175/2008MWR2596.1).

967 Kruse, C. G., and R. B. Smith, 2015: Gravity wave diagnostics and characteristics in mesoscale
968 fields. *J. Atmos. Sci.*, **72**, 4372–4392, doi:10.1175/JAS-D-15-0079.1, URL [http://dx.doi.org/10.
1175/JAS-D-15-0079.1](http://dx.doi.org/10.
969 1175/JAS-D-15-0079.1).

970 Kruse, C. G., R. B. Smith, and S. D. Eckermann, 2016: The midlatitude lower-stratospheric
971 mountain wave valve layer. *J. Atmos. Sci.*, **73**, 5081–5100, doi:10.1175/JAS-D-16-0173.1, URL
972 <http://dx.doi.org/10.1175/JAS-D-16-0173.1>.

973 Kühnlein, C., A. Dörnbrack, and M. Weissmann, 2013: High-resolution Doppler lidar ob-
974 servations of transient downslope flows and rotors. *Mon. Wea. Rev.*, **141**, 3257–3272, doi:
975 10.1175/MWR-D-12-00260.1, URL <http://dx.doi.org/10.1175/MWR-D-12-00260.1>.

976 Lane, T. P., M. J. Reeder, B. R. Morton, and T. L. Clark, 2000: Observations and numerical
977 modelling of mountain waves over the Southern Alps of New Zealand. *Quart. J. Roy. Me-
978 teor. Soc.*, **126**, 2765–2788, doi:10.1002/qj.49712656909, URL [http://dx.doi.org/10.1002/qj.
979 49712656909](http://dx.doi.org/10.1002/qj.49712656909).

980 Liu, Y., X. San Liang, and R. H. Weisberg, 2007: Rectification of the bias in the wavelet power
981 spectrum. *J. Atmos. Oceanic Technol.*, **24**, 2093–2102, doi:10.1175/2007JTECHO511.1, URL
982 <http://dx.doi.org/10.1175/2007JTECHO511.1>.

983 Lott, F., and H. Teitelbaum, 1993a: Linear unsteady mountain waves. *Tellus A*, **45**, 201–220, doi:
984 10.1034/j.1600-0870.1993.t01-2-00004.x, URL [http://dx.doi.org/10.1034/j.1600-0870.1993.
985 t01-2-00004.x](http://dx.doi.org/10.1034/j.1600-0870.1993.t01-2-00004.x).

986 Lott, F., and H. Teitelbaum, 1993b: Topographic waves generated by a transient wind. *J. Atmos.
987 Sci.*, **50**, 2607–2624, doi:10.1175/1520-0469(1993)050<2607:TWGBAT>2.0.CO;2, URL [http:
988 //dx.doi.org/10.1175/1520-0469\(1993\)050<2607:TWGBAT>2.0.CO;2](http://dx.doi.org/10.1175/1520-0469(1993)050<2607:TWGBAT>2.0.CO;2).

989 Martin, A., and F. Lott, 2007: Synoptic responses to mountain gravity waves encountering
990 directional critical levels. *J. Atmos. Sci.*, **64**, 828–848, doi:10.1175/JAS3873.1, URL [https:
991 //doi.org/10.1175/JAS3873.1](https://doi.org/10.1175/JAS3873.1).

- 992 Menchaca, M. Q., and D. R. Durran, 2017: Mountain waves, downslope winds, and low-level
993 blocking forced by a midlatitude cyclone encountering an isolated ridge. *J. Atmos. Sci.*, **74**,
994 617–639, doi:10.1175/JAS-D-16-0092.1, URL <https://doi.org/10.1175/JAS-D-16-0092.1>.
- 995 Pautet, P.-D., M. J. Taylor, W. R. P. Jr., Y. Zhao, T. Yuan, R. Esplin, and D. McLain, 2014: An
996 advanced mesospheric temperature mapper for high-latitude airglow studies. *Appl. Optics*, **53**,
997 5934–5943.
- 998 Pautet, P.-D., and Coauthors, 2016: Large-amplitude mesospheric response to an orographic wave
999 generated over the Southern Ocean Auckland Islands (50.7°S) during the DEEPWAVE project.
1000 *J. Geophys. Res.*, **121**, 1431–1441, doi:10.1002/2015JD024336, URL [http://dx.doi.org/10.1002/](http://dx.doi.org/10.1002/2015JD024336)
1001 2015JD024336.
- 1002 Queney, P., 1948: The problem of air flow over mountains: A summary of theoretical results. *Bull.*
1003 *Amer. Meteor. Soc.*, **29**, 16–26.
- 1004 Reeder, M. J., N. Adams, and T. P. Lane, 1999: Radiosonde observations of partially trapped
1005 lee waves over Tasmania, Australia. *J. Geophys. Res.*, **104**, 16 719–16 727, doi:10.1029/
1006 1999JD900038, URL <http://dx.doi.org/10.1029/1999JD900038>.
- 1007 Ross, S. M., Ed., 2009: *Introduction to Probability and Statistics for Engineers and Scientists*.
1008 4th ed., Academic Press, Boston, 664 pp., doi:[http://dx.doi.org/10.1016/B978-0-12-370483-2.](http://dx.doi.org/10.1016/B978-0-12-370483-2.50002-2)
1009 50002-2, URL <http://www.sciencedirect.com/science/article/pii/B9780123704832500022>.
- 1010 Rotering, H., 2011: Falcon 20-E5 trailing cone validation. Institute Report IB 111-2011/28, Ger-
1011 man Aerospace Center, Institute of Flight Systems, Flight Test Branch, Flight Experiments.
- 1012 Scorer, R. S., 1949: Theory of waves in the lee of mountains. *Quart. J. Roy. Meteor. Soc.*, **75**,
1013 41–46.

1014 Skamarock, W. C., and J. B. Klemp, 2008: A time-split nonhydrostatic atmospheric model for
1015 weather research and forecasting applications. *J. Comp. Phys.*, **227**, 3465 – 3485, doi:<http://dx.doi.org/10.1016/j.jcp.2007.01.037>, URL [http://www.sciencedirect.com/science/article/pii/](http://www.sciencedirect.com/science/article/pii/S0021999107000459)
1016 [S0021999107000459](http://www.sciencedirect.com/science/article/pii/S0021999107000459).
1017

1018 Skamarock, W. C., and Coauthors, 2008: A description of the advanced research WRF version 3.
1019 *NCAR Techn. Notes, NCAR/TN-475+STR*, 113 pp, doi:[doi:10.5065/D68S4MVH](https://doi.org/10.5065/D68S4MVH).

1020 Smith, R. B., 1979: The influence of the mountains on the atmosphere. *Adv. Geophys.*, **21**, 87–230.

1021 Smith, R. B., J. D. Doyle, Q. Jiang, and S. A. Smith, 2007: Alpine gravity waves: Lessons from
1022 MAP regarding mountain wave generation and breaking. *Quart. J. Roy. Meteor. Soc.*, **133**, 917–
1023 936, doi:[10.1002/qj.103](https://doi.org/10.1002/qj.103), URL <http://dx.doi.org/10.1002/qj.103>.

1024 Smith, R. B., and C. G. Kruse, 2017: Broad-spectrum mountain waves. *J. Atmos. Sci.*, **74**, 1381–
1025 1402, doi:[10.1175/JAS-D-16-0297.1](https://doi.org/10.1175/JAS-D-16-0297.1), URL <https://doi.org/10.1175/JAS-D-16-0297.1>, [https://](https://doi.org/10.1175/JAS-D-16-0297.1)
1026 doi.org/10.1175/JAS-D-16-0297.1.

1027 Smith, R. B., B. K. Woods, J. Jensen, W. A. Cooper, J. D. Doyle, Q. Jiang, and V. Grubišić,
1028 2008: Mountain waves entering the stratosphere. *J. Atmos. Sci.*, **65**, 2543–2562, doi:[10.1175/](https://doi.org/10.1175/2007JAS2598.1)
1029 [2007JAS2598.1](https://doi.org/10.1175/2007JAS2598.1), URL <http://dx.doi.org/10.1175/2007JAS2598.1>.

1030 Smith, R. B., and Coauthors, 2016: Stratospheric gravity wave fluxes and scales during DEEP-
1031 WAVE. *J. Atmos. Sci.*, **73**, 2851–2869, doi:[10.1175/JAS-D-15-0324.1](https://doi.org/10.1175/JAS-D-15-0324.1), URL [http://dx.doi.org/](http://dx.doi.org/10.1175/JAS-D-15-0324.1)
1032 [10.1175/JAS-D-15-0324.1](http://dx.doi.org/10.1175/JAS-D-15-0324.1).

1033 Smith, S., J. Baumgardner, and M. Mendillo, 2009: Evidence of mesospheric gravity-waves
1034 generated by orographic forcing in the troposphere. *Geophys. Res. Lett.*, **36** (8), doi:[10.1029/](https://doi.org/10.1029/2008GL036936)
1035 [2008GL036936](https://doi.org/10.1029/2008GL036936), URL <http://dx.doi.org/10.1029/2008GL036936>.

- 1036 Strauss, L., S. Serafin, and V. Grubišić, 2016: Atmospheric rotors and severe turbulence in a long
1037 deep valley. *J. Atmos. Sci.*, **73**, 1481–1506, doi:10.1175/JAS-D-15-0192.1, URL <http://dx.doi.org/10.1175/JAS-D-15-0192.1>,
1038 <http://dx.doi.org/10.1175/JAS-D-15-0192.1>.
- 1039 Teixeira, M. A. C., 2014: The physics of orographic gravity wave drag. *Frontiers in Physics*, **2**,
1040 43, doi:10.3389/fphy.2014.00043, URL [http://journal.frontiersin.org/article/10.3389/fphy.2014.](http://journal.frontiersin.org/article/10.3389/fphy.2014.00043)
1041 00043.
- 1042 Torrence, C., and G. P. Compo, 1998: A practical guide to wavelet analysis. *Bull. Amer. Meteor.*
1043 *Soc.*, **79**, 61–78, doi:10.1175/1520-0477(1998)079<0061:APGTWA>2.0.CO;2, URL [http://dx.](http://dx.doi.org/10.1175/1520-0477(1998)079<0061:APGTWA>2.0.CO;2)
1044 [doi.org/10.1175/1520-0477\(1998\)079<0061:APGTWA>2.0.CO;2](http://dx.doi.org/10.1175/1520-0477(1998)079<0061:APGTWA>2.0.CO;2).
- 1045 Wagner, J., and Coauthors, 2017: Observed versus simulated mountain waves over Scandi-
1046 navia – improvement of vertical winds, energy and momentum fluxes by enhanced model
1047 resolution? *Atmos. Chem. Phys.*, **17**, 4031–4052, doi:10.5194/acp-17-4031-2017, URL [https:](https://www.atmos-chem-phys.net/17/4031/2017/)
1048 [//www.atmos-chem-phys.net/17/4031/2017/](https://www.atmos-chem-phys.net/17/4031/2017/).
- 1049 Wallace, L., 1962: The OH nightglow emission. *J. Atmos. Sci.*, **19**, 1–16.
- 1050 Woods, B. K., and R. B. Smith, 2010a: Energy flux and wavelet diagnostics of secondary mountain
1051 waves. *J. Atmos. Sci.*, **67**, 3721–3738, doi:10.1175/2009JAS3285.1, URL [http://dx.doi.org/10.](http://dx.doi.org/10.1175/2009JAS3285.1)
1052 [1175/2009JAS3285.1](http://dx.doi.org/10.1175/2009JAS3285.1).
- 1053 Woods, B. K., and R. B. Smith, 2010b: Short-wave signatures of stratospheric mountain wave
1054 breaking. *J. Atmos. Sci.*, **68**, 635–656, doi:10.1175/2010JAS3634.1, URL [http://dx.doi.org/10.](http://dx.doi.org/10.1175/2010JAS3634.1)
1055 [1175/2010JAS3634.1](http://dx.doi.org/10.1175/2010JAS3634.1).

1056 **LIST OF TABLES**

1057 **Table 1.** Identified mountains along the Mt.-Aspiring-2b transect from West to East with
 1058 their respective latitudes and longitudes. The letters and distances refer to the
 1059 marked peaks in Fig. 3a and their respective distance to the reference point
 1060 (middle of the island along the cross-section). 48

1061 **Table 2.** Serial leg numbers as counted in Fig. 2, research flight (RF: GV, FF: Fal-
 1062 con), flight leg number, respective forcing phase (*accelerating*, *maximum*,
 1063 *decelerating*), day, mean leg time, leg-averaged flight altitude, flight transect
 1064 (*Mt. Aspiring*, *Mt. Cook*) and status of cross-mountain legs during DEEP-
 1065 WAVE IOP 9. A checkmark in the status column is provided for Mt.-Aspiring-
 1066 2b flight legs that were analyzed in more detail in this paper. 49

	Distance	Name	Latitude	Longitude
A	≈ -95 km	Part of the Climax Peak	44.33°S	168.47°E
B	≈ -70 km	Mount Aspiring	44.45°S	168.74°E
C	≈ -45 km	Mount Alta	44.57°S	169.00°E
D	≈ 20 km	Dunstan Mountains	44.87°S	169.69°E
E	≈ 90 km	Part of Mount Pisgah	45.18°S	170.44°E

1067 TABLE 1. Identified mountains along the Mt.-Aspiring-2b transect from West to East with their respective
1068 latitudes and longitudes. The letters and distances refer to the marked peaks in Fig. 3a and their respective
1069 distance to the reference point (middle of the island along the cross-section).

Serial N ^o	Flight	Leg N ^o	Forcing Phase	Day	Mean Time	Mean Altitude	Transect	Status
1	RF11	1	Acc	28-6	06:37 UTC	12.1 km	Mt-C-1b	
2	RF11	8	Acc	28-6	11:23 UTC	12.1 km	Mt-C-1b	
3	RF12	1	Max I	29-6	08:38 UTC	12.1 km	Mt-A-2b	✓
4	RF12	3	Max I	29-6	09:15 UTC	12.1 km	Mt-C-1b	
5	RF12	6	Max I	29-6	11:08 UTC	12.0 km	Mt-A-2b	✓
6	RF12	8	Max I	29-6	11:45 UTC	12.1 km	Mt-C-1b	
7	RF12	10	Max I	29-6	12:23 UTC	12.7 km	Mt-A-2b	✓
8	RF12	12	Max I	29-6	12:59 UTC	12.7 km	Mt-C-1b	
9	RF12	14	Max II	29-6	13:36 UTC	12.1 km	Mt-A-2b	✓
10	RF12	16	Max II	29-6	14:13 UTC	12.1 km	Mt-C-1b	
11	RF12	18	Max II	29-6	14:51 UTC	13.3 km	Mt-A-2b	✓
12	RF12	20	Max II	29-6	15:26 UTC	13.3 km	Mt-C-1b	
13	RF12	22	Max II	29-6	16:03 UTC	13.6 km	Mt-A-2b	✓
14	RF12	24	Max II	29-6	16:26 UTC	13.6 km	Mt-C-1b	
15	FF01	1	Early Dec	29-6	23:30 UTC	7.7 km	Mt-A-2b different	
16	FF01	2	Early Dec	30-6	00:14 UTC	8.9 km	Mt-A-2b	✓
17	FF01	3	Early Dec	30-6	00:57 UTC	10.7 km	Mt-A-2b	✓
18	FF01	4	Early Dec	30-6	01:37 UTC	9.7 km	Mt-A-2b	✓
19	RF13	1	Mid Dec	30-6	06:35 UTC	11.9 km	Mt-A-2b	✓
20	RF13	3	Mid Dec	30-6	07:11 UTC	11.9 km	Mt-C-1b	
21	RF13	6	Mid Dec	30-6	09:03 UTC	11.9 km	Mt-A-2b	✓
22	RF13	8	Mid Dec	30-6	09:39 UTC	11.9 km	Mt-C-1b	
23	RF13	10	Mid Dec	30-6	10:16 UTC	11.9 km	Mt-A-2b	✓
24	RF13	12	Mid Dec	30-6	10:53 UTC	11.9 km	Mt-C-1b	
25	RF13	13	Mid Dec	30-6	11:30 UTC	13.3 km	Mt-A-2b	✓
26	RF13	15	Mid Dec	30-6	12:06 UTC	13.4 km	Mt-C-1b	
27	RF13	17	Mid Dec	30-6	12:43 UTC	13.3 km	Mt-A-2b	✓
28	RF13	19	Late Dec	30-6	13:19 UTC	13.4 km	Mt-C-1b	
29	RF13	21	Late Dec	30-6	13:57 UTC	11.9 km	Mt-A-2b	✓
30	RF13	23	Late Dec	30-6	14:34 UTC	11.9 km	Mt-C-1b	
31	FF02	1	Late Dec	30-6	16:54 UTC	7.6 km	Mt-A-2b	✓
32	FF02	2	Late Dec	30-6	17:41 UTC	8.8 km	Mt-A-2b	✓
33	FF02	3	Late Dec	30-6	18:22 UTC	10.6 km	Mt-A-2b	✓
34	FF02	4	Late Dec	30-6	19:09 UTC	11.5 km	Mt-A-2b	✓
35	RF14	1	Late Dec	1-7	06:43 UTC	11.8 km	Mt-C-1a	
36	RF14	2	Late Dec	1-7	07:22 UTC	11.8 km	Mt-C-1a	
37	RF14	3	Late Dec	1-7	08:02 UTC	11.8 km	Mt-C-1a	
38	RF14	6	Late Dec	1-7	10:00 UTC	11.8 km	Mt-C-1a	
39	RF14	7	Late Dec	1-7	10:40 UTC	8.7 km	Mt-C-1a	
40	RF14	8	Late Dec	1-7	11:23 UTC	11.8 km	Mt-C-1a	
41	RF14	9	Late Dec	1-7	12:04 UTC	13.4 km	Mt-C-1a	

1070 TABLE 2. Serial leg numbers as counted in Fig. 2, research flight (RF: GV, FF: Falcon), flight leg number,
1071 respective forcing phase (*accelerating, maximum, decelerating*), day, mean leg time, leg-averaged flight altitude,
1072 flight transect (*Mt. Aspiring, Mt. Cook*) and status of cross-mountain legs during DEEPWAVE IOP 9. A
1073 checkmark in the status column is provided for Mt.-Aspiring-2b flight legs that were analyzed in more detail in
1074 this paper.

1075

LIST OF FIGURES

- 1076 **Fig. 1.** Map of the South Island of New Zealand with colored flight transects Mount Cook 1a and
 1077 1b, Mount Aspiring 2b, the radiosonde stations Haast and Lauder and the radiosonde flight
 1078 tracks during the IOP 9. The thin red line close to Mt.-Aspiring-2b flight transect marks
 1079 FF01 leg 1. In addition, the upstream point (44.2° S, 167.5° E) used in the ECMWF analyses
 1080 is shown. Triangles denote the location of Mt. Aspiring and Mt. Cook in the respective color
 1081 coding. 53
- 1082 **Fig. 2.** ECMWF IFS Brunt-Vaisala frequency (N^2) with colored contours of $\geq 6 \cdot 10^{-4} \text{ s}^{-2}$ in red
 1083 and $\leq 0.5 \cdot 10^{-4} \text{ s}^{-2}$ in blue. Grey shaded are areas of $N^2 \leq 3 \cdot 10^{-4} \text{ s}^{-2}$. The brown dashed
 1084 line, the orange normal and green diagonal crosses give the thermal tropopause calculated
 1085 from IFS data, as well as from Haast and Lauder soundings, respectively. Blue and red rect-
 1086 angles show altitudes of all GV and Falcon mountain legs. Dotted-dashed vertical lines are
 1087 the separation into accelerating, maximum and decelerating forcing phases. Dotted vertical
 1088 lines further show the division into maximum forcing phase I and II, and early, mid and late
 1089 decelerating forcing phases. 54
- 1090 **Fig. 3.** (a) WRF topography with the finest obtainable resolution of 30 arc seconds along the Mt.-
 1091 Aspiring-2b transect with labelled peaks. For the projection upon the flight tracks, the Lam-
 1092 bert projection is used, with a 1 km grid spacing and the topography data bilinearly interpo-
 1093 lated to the flight track coordinates. The middle of the island along the transect is taken as
 1094 the reference point (distance = 0 km). (b) Map over the South Island of New Zealand with
 1095 the identified mountains along the Mt.-Aspiring-2b transect (GOOGLE 2015, Earth View). 55
- 1096 **Fig. 4.** Hovmoeller diagram of the meridional wind component (m s^{-1}) at 700 hPa obtained from
 1097 the ECMWF IFS. Data were spatially averaged between 40° to 45° S. The dashed lines mark
 1098 the location of the SI. Black contour lines are shown for 12, 24 and 48 m s^{-1} . DL in the
 1099 longitude-axis marks the date line. 56
- 1100 **Fig. 5.** (a, c, e) ECMWF IFS equivalent potential temperature and (b, d, f) horizontal wind with
 1101 wind barbs and 20-m-spaced contours of geopotential height at 700 hPa for 29 June at
 1102 12 UTC, and 30 June 2014 at 00 and 12 UTC. The transect Mt.-Aspiring-2b is superim-
 1103 posed as black line in the individual panels. The location of Mt. Aspiring (MA) is marked
 1104 with a red dot. 57
- 1105 **Fig. 6.** ECMWF IFS upstream cross-mountain wind speed (at 44.2° S, 167.5° E) during IOP 9
 1106 from 00 UTC 28 June till 06 UTC 01 July 2014. Mean upstream values were calculated
 1107 as averages over the lowest 4 km (blue). Green and orange triangles depict the respective
 1108 values for the Lauder and Haast sondes. Up to 5 m s^{-1} wind speed, the forcing is referred
 1109 to as “weak”, from 5 to 15 m s^{-1} as “moderate” and more than 15 m s^{-1} as “strong”.
 1110 The dotted-dashed vertical lines refer to the division into accelerating, maximum and de-
 1111 celerating forcing. Also periods of synoptic events, like passing fronts and convection are
 1112 marked. The dashed black curve marks an approximation of the transient forcing following
 1113 $U_{\perp}(t) = U_{\perp 0} + \Delta U_{\perp} \cos^2(\pi t / t_{tot})$ with $U_{\perp 0} = 5 \text{ m s}^{-1}$, $\Delta U_{\perp} = 17 \text{ m s}^{-1}$ and $t_{tot} = 53 \text{ h}$ 58
- 1114 **Fig. 7.** ECMWF IFS horizontal wind speed with wind barbs and 40-m-spaced contours of geopo-
 1115 tential height at (a) 300 hPa and (b) 200 hPa at 00 UTC 29 June 2014, (c) 300 hPa and (d)
 1116 200 hPa at 00 UTC 30 June 2014, (e) 300 hPa and (f) 200 hPa at 12 UTC 30 June 2014. 59
- 1117 **Fig. 8.** ECMWF IFS upstream (a) cross-mountain wind speed and (b) Scorer parameter smoothed
 1118 over 750 m in the vertical during 3-hour windows of maximum forcing phase part I (06/29
 1119 08 - 10 UTC), part II (06/29 14 - 16 UTC), early (06/29 23 - 01 UTC) and late (06/30 17 -

1120 19 UTC) decelerating forcing phases. In red, the critical wavenumbers and wavelengths for
 1121 propagation based on an argument from steady-state theory are given for different periods
 1122 (b). Waves are able to propagate as long as the ambient Scorer parameter is larger than
 1123 the selected wavenumber. From bottom to top, the altitude range of inhibited propagation
 1124 for waves shorter than 50 km horizontal wavelength during maximum forcing phase part I
 1125 (06/29 08 - 10 UTC), of strong negative shear during maximum forcing phase part II (06/29
 1126 14 - 16 UTC) and during early decelerating forcing phase (06/29 23 - 01 UTC) are shaded
 1127 in grey. 60

1128 **Fig. 9.** WRF vertical wind along the Mt.-Aspiring-2b transect up to 33 km altitude (sponge layer is
 1129 excluded) with 5-K-spaced isentropes up to 320 K and 10-K-spaced isentropes above at (a)
 1130 09 UTC, (b) 15 UTC, (c) 23 UTC 29 June and (d) 18 UTC 30 June. 61

1131 **Fig. 10.** Vertical displacement for the flight legs of (a) RF12 and (b) FF01 on 29 June 2014, (c)
 1132 RF13 and (d) FF02 on 30 June 2014 with underlying topography along the Mt.-Aspiring-2b
 1133 transect. For the Falcon legs, the topography originates from the WRF model with the finest
 1134 obtainable resolution of 30 arc seconds. For the GV flight tracks, the topographic height was
 1135 provided by the Earth Observing Laboratory (NCAR EOL). In (b), an estimated phase line
 1136 (black) of the long waves ($\lambda_x \approx 200$ km) is shown to guide the eye. 62

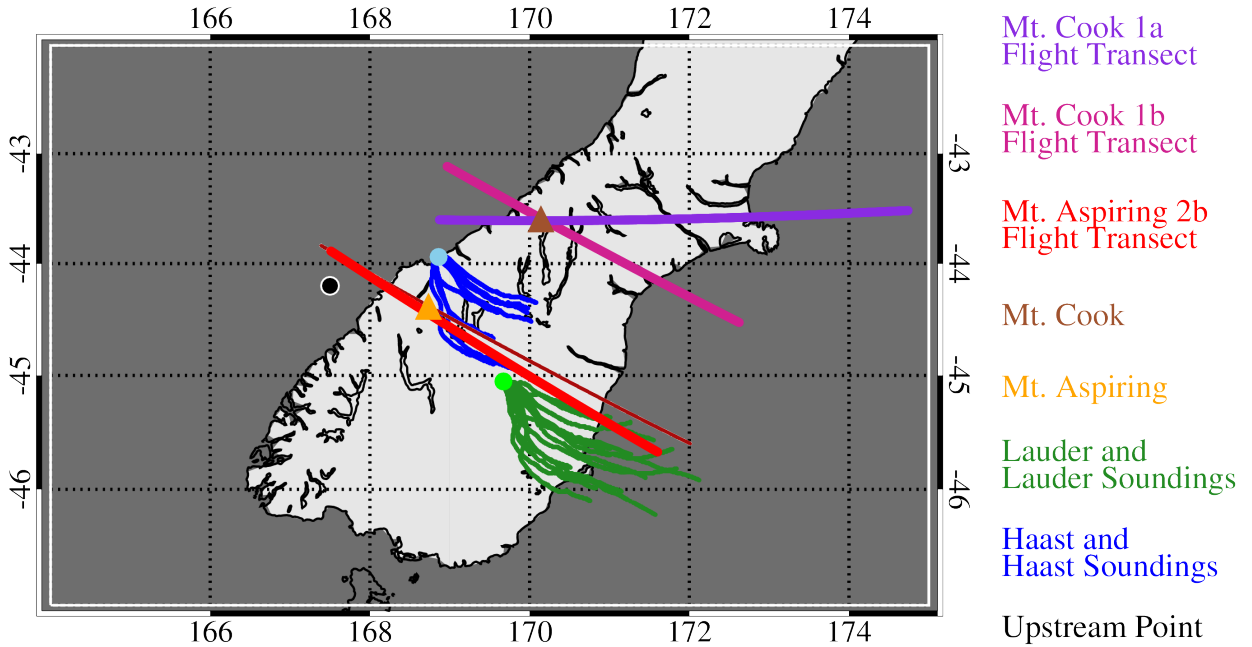
1137 **Fig. 11.** (a) Time series of leg-integrated vertical flux of along-track momentum ($-MF_{track}$) for the
 1138 GV (RF12 and RF13) and Falcon (FF01 and FF02) aircraft for all Mt.-Aspiring-2b legs,
 1139 as well as of simulated flux values of the WRF model smoothed over 3 h along the Mt.-
 1140 Aspiring-2b transect at typical flight altitudes of 8 and 13 km. As in Fig. 2 and 6, the
 1141 divisions into accelerating, part I and II of maximum, early, mid and late decelerating
 1142 forcing phases are marked with vertical lines. In addition, minimum, mean and maximum $-MF_{track}$ -
 1143 values at 8 (black) and 13 km (light blue) altitude of 6 quasi-steady WRF runs with constant
 1144 background profiles initialized at 00, 06, 12 and 18 UTC on 29 June and at 00 and 06 UTC
 1145 on 30 June are shown as error bars (also see Fig. 13). In (b) and in (c), the same is shown
 1146 as in (a), but only for signal parts including wavelengths larger and smaller than 30 km,
 1147 respectively. 63

1148 **Fig. 12.** Test of the linear Eliassen-Palm relation between the energy flux (EF_z) and the scalar product
 1149 of horizontal wind ($\mathbf{U} = [u, v]$) and the horizontal momentum flux ($\mathbf{MF} = [MF_x, MF_y]$) for
 1150 all Mt.-Aspiring-2b legs during IOP 9 and the WRF simulations along the Mt.-Aspiring-2b
 1151 transect at 8 and 13 km altitude. The solid lines represent the linear regression of EF_z and
 1152 $\mathbf{U} \cdot \mathbf{MF}$ for WRF at 8 km altitude (black), at 13 km altitude (light blue) and the airborne
 1153 observations of the Mt.-Aspiring-2b legs (red). Further given are the respective functions of
 1154 the linear regression and the squared Pearson correlation coefficient R^2 64

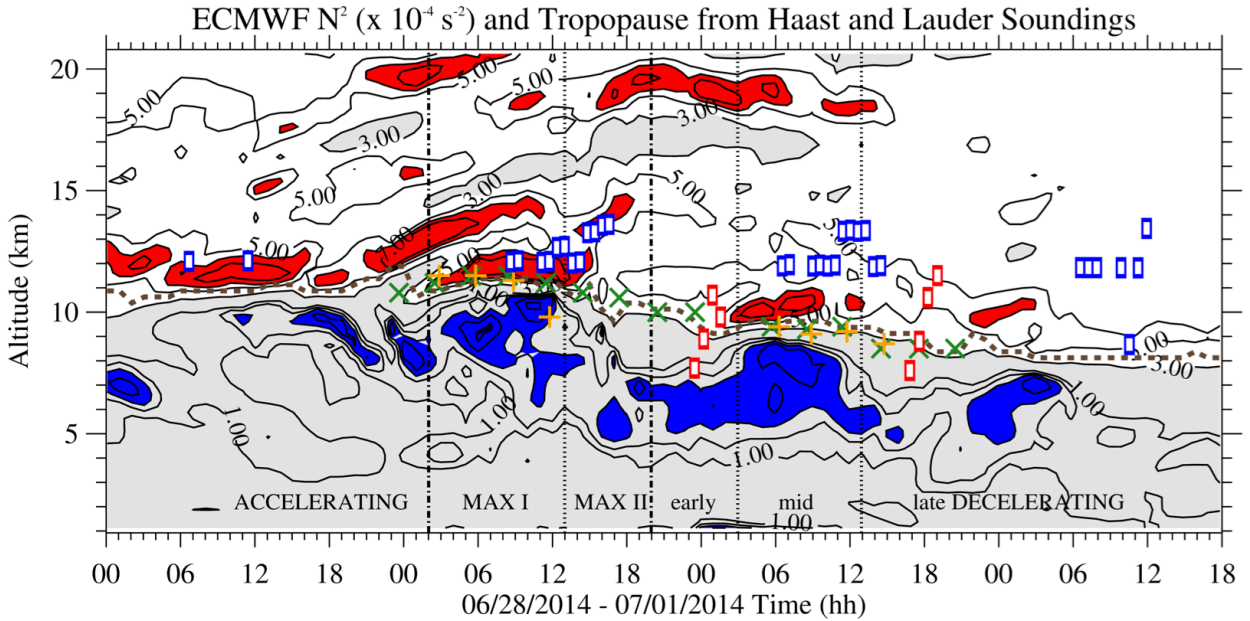
1155 **Fig. 13.** WRF leg-integrated 3-h-smoothed vertical flux of along-track momentum of quasi-steady
 1156 runs at 13 km altitude as a function of run time after the respective initialization. All runs
 1157 were simulated for 48 hours. The light gray shading gives the time interval (30 - 48 hours
 1158 run time) during which the simulations are assumed to reach a quasi steady-state. This time
 1159 interval is used to average the flux values and to compare to the “transient” WRF simulation
 1160 and the observations in Fig. 11. 65

1161 **Fig. 14.** (a) $EF_{zn}(s_j)$ (vertical energy flux) and (b) $MF_{trackn}(s_j)$ (along-track momentum flux) wavelet
 1162 cospectra with underlying topography for the GV RF12 leg 6 on 29 June 2014 during max-
 1163 imum forcing phase of the IOP 9. The hatched area is significant on the 5%-level and the
 1164 surrounding solid black line represents the 95% confidence limit. The cross-hatched area
 1165 gives the cone of influence. In (c) and (d) the same is shown as in (a) and (b), but for GV
 1166 RF12 leg 22, respectively. 66

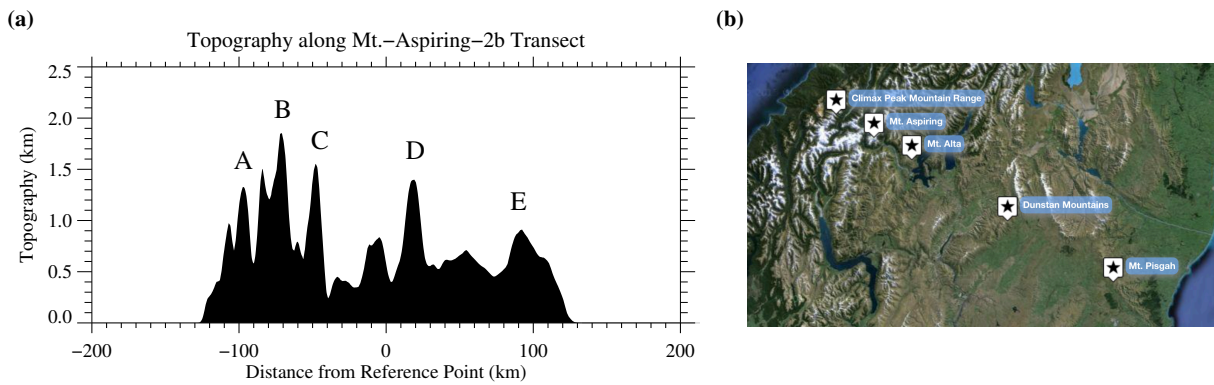
1167	Fig. 15.	(a), (b) and (c), (d) same as in Fig. 14a, b but for Falcon FF01 leg 2 on 29 June and leg 4 on	
1168		30 June 2014 during early decelerating forcing phase of the IOP 9.	67
1169	Fig. 16.	(a), (b) and (c), (d) same as in Fig. 14a, b but for Falcon FF02 leg 2 and 3 on 30 June during	
1170		late decelerating forcing phase of the IOP 9. Note the different limits of the distance-axis	
1171		for leg 3 in (c) and (d).	68
1172	Fig. 17.	Density-corrected, approximated vertical velocity fluctuation and potential temperature of	
1173		the radiosoundings launched at Lauder on 29 June (a) 11:29 UTC (maximum forcing phase	
1174		part I), (b) 17:25 UTC (maximum forcing phase part II), (c) 23:33 UTC (early decelerating	
1175		forcing) and on (d) 30 June 20:35 UTC (late decelerating forcing). Density-corrected refers	
1176		to the multiplication of w' by the factor $(\rho(z)/\rho(z=0))^{1/2}$ to remove the effect of exponen-	
1177		tially amplifying w' with height due to decreasing density ρ . The flight passages within the	
1178		troposphere, tropopause and stratosphere are colored in blue, green and violet, respectively.	
1179		Gray shaded are layers where $-0.06 < \partial\theta/\partial z < 0.09 \text{ K km}^{-1}$	69
1180	Fig. 18.	One-hourly mean of gravity wave potential energy density (GWPED), logarithmically aver-	
1181		aged over the upper stratosphere (violet dots), stratopause (black dots) and mesosphere (blue	
1182		dots). In addition, the thin dotted lines denote the 1-hourly running mean of the 2-min GW-	
1183		PED data during the Rayleigh lidar measurement at Lauder, New Zealand, on 30 June. In	
1184		general, the GWPED increases with height due to wave amplification with decreasing air	
1185		density.	70
1186	Fig. 19.	Keograms (time-distance sections constructed from collocated time series of narrow AMTM	
1187		image slices) of the AMTM observations during (a) RF12 on 29 June and (b) RF13 on	
1188		30 June 2014.	71



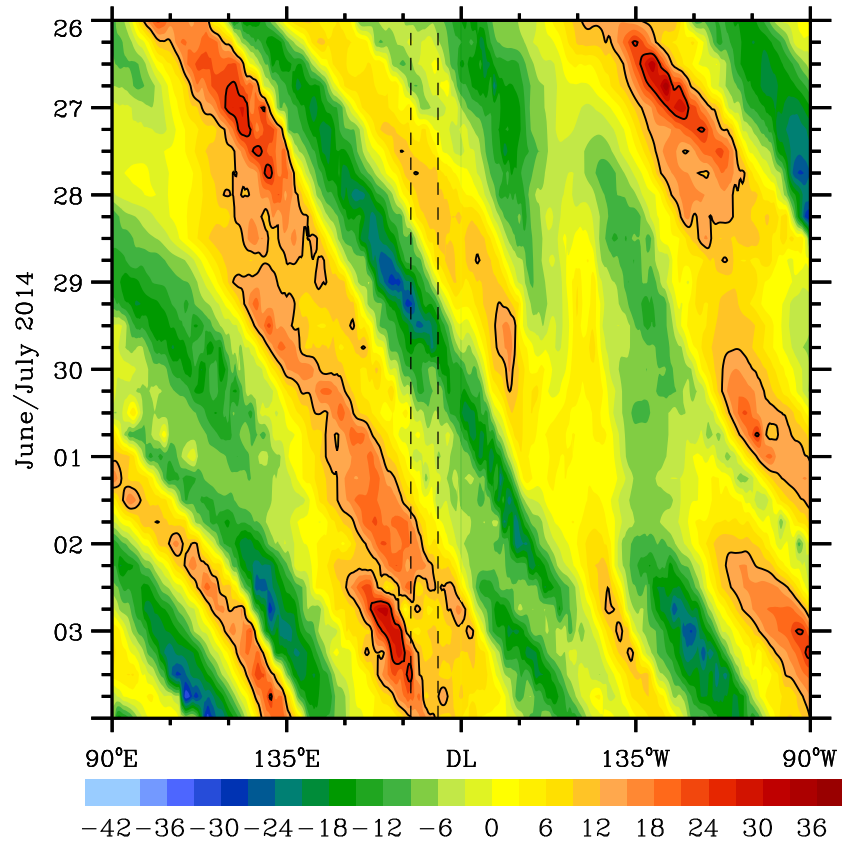
1189 FIG. 1. Map of the South Island of New Zealand with colored flight transects Mount Cook 1a and 1b, Mount
 1190 Aspiring 2b, the radiosonde stations Haast and Lauder and the radiosonde flight tracks during the IOP 9. The
 1191 thin red line close to Mt.-Aspiring-2b flight transect marks FF01 leg 1. In addition, the upstream point (44.2° S,
 1192 167.5° E) used in the ECMWF analyses is shown. Triangles denote the location of Mt. Aspiring and Mt. Cook
 1193 in the respective color coding.



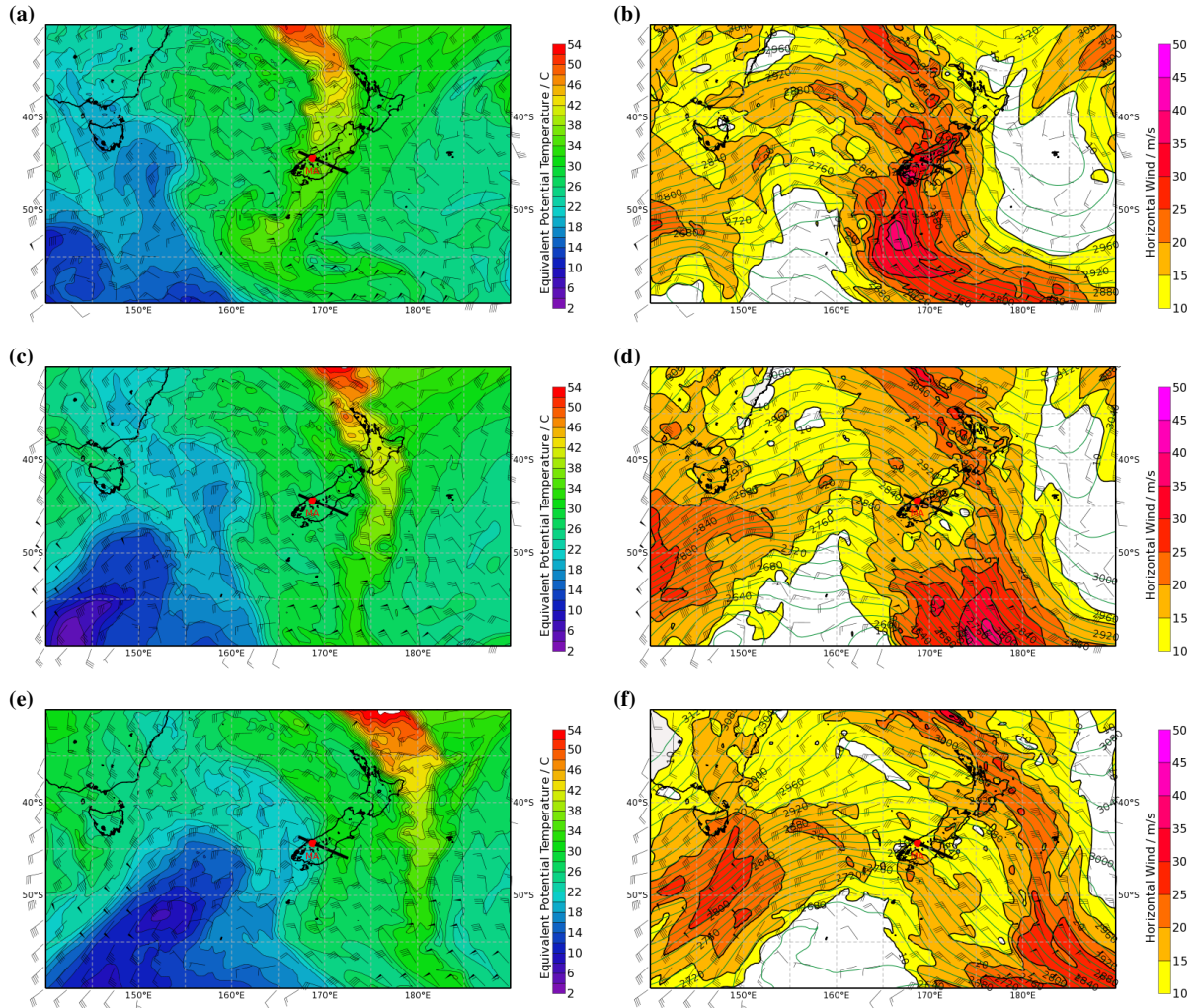
1194 FIG. 2. ECMWF IFS Brunt-Vaisala frequency (N^2) with colored contours of $\geq 6 \cdot 10^{-4} \text{ s}^{-2}$ in red and
 1195 $\leq 0.5 \cdot 10^{-4} \text{ s}^{-2}$ in blue. Grey shaded are areas of $N^2 \leq 3 \cdot 10^{-4} \text{ s}^{-2}$. The brown dashed line, the orange normal
 1196 and green diagonal crosses give the thermal tropopause calculated from IFS data, as well as from Haast and
 1197 Lauder soundings, respectively. Blue and red rectangles show altitudes of all GV and Falcon mountain legs.
 1198 Dotted-dashed vertical lines are the separation into accelerating, maximum and decelerating forcing phases.
 1199 Dotted vertical lines further show the division into maximum forcing phase I and II, and early, mid and late
 1200 decelerating forcing phases.



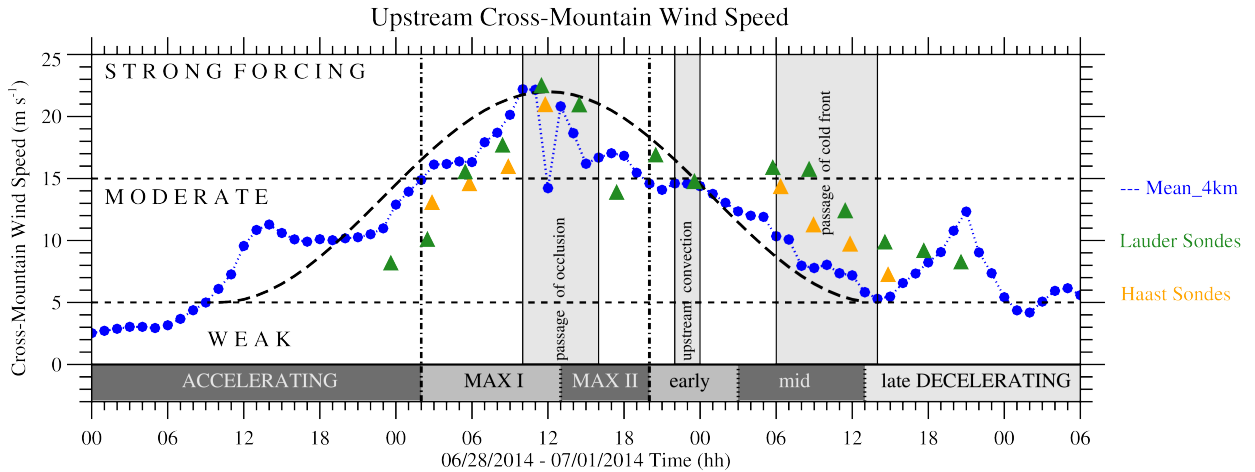
1201 FIG. 3. (a) WRF topography with the finest obtainable resolution of 30 arc seconds along the Mt.-Aspiring-2b
 1202 transect with labelled peaks. For the projection upon the flight tracks, the Lambert projection is used, with a
 1203 1 km grid spacing and the topography data bilinearly interpolated to the flight track coordinates. The middle of
 1204 the island along the transect is taken as the reference point (distance = 0 km). (b) Map over the South Island of
 1205 New Zealand with the identified mountains along the Mt.-Aspiring-2b transect (GOOGLE 2015, Earth View).



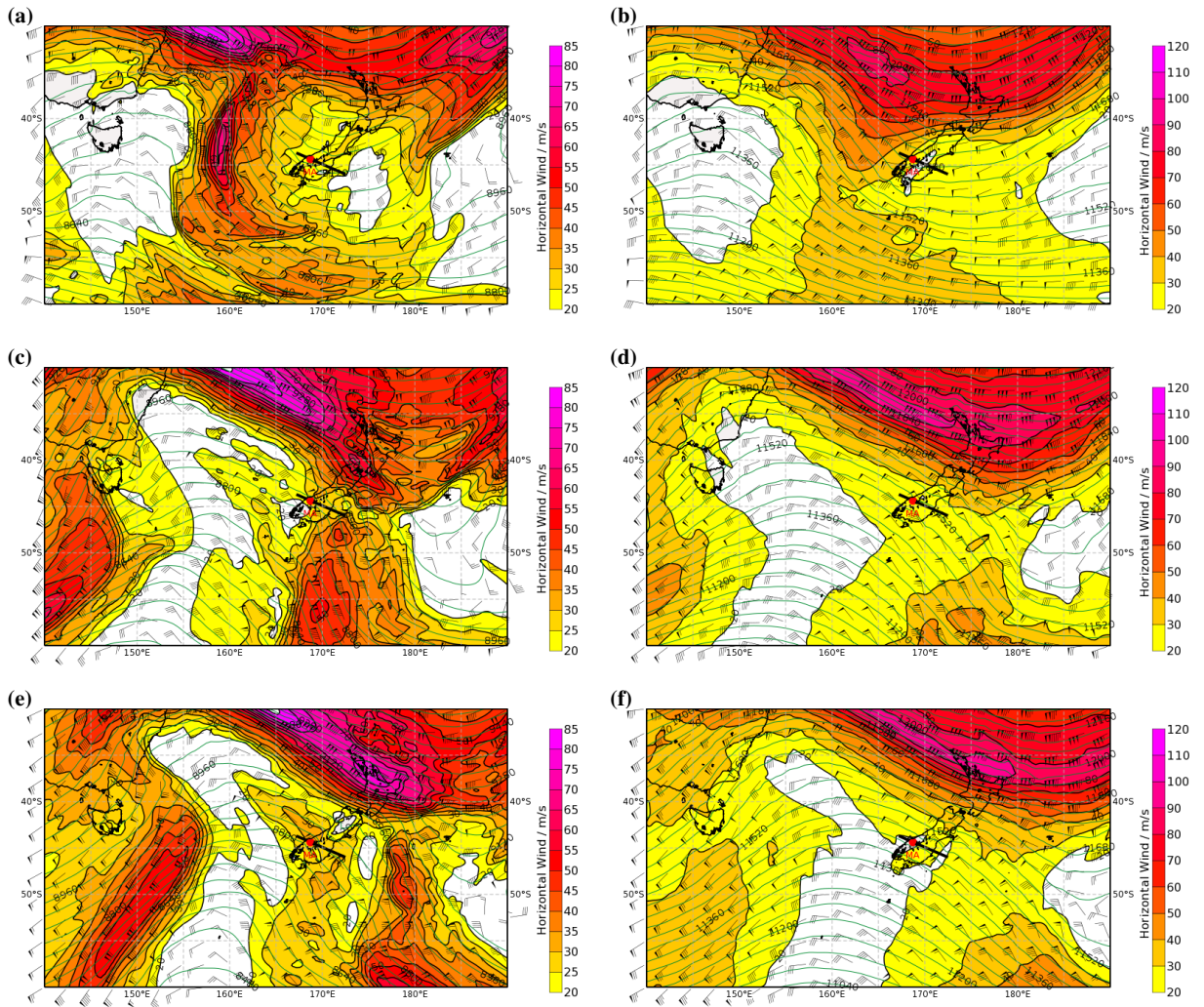
1206 FIG. 4. Hovmoeller diagram of the meridional wind component (m s^{-1}) at 700 hPa obtained from the ECMWF
 1207 IFS. Data were spatially averaged between 40° to 45° S. The dashed lines mark the location of the SI. Black
 1208 contour lines are shown for 12, 24 and 48 m s^{-1} . DL in the longitude-axis marks the date line.



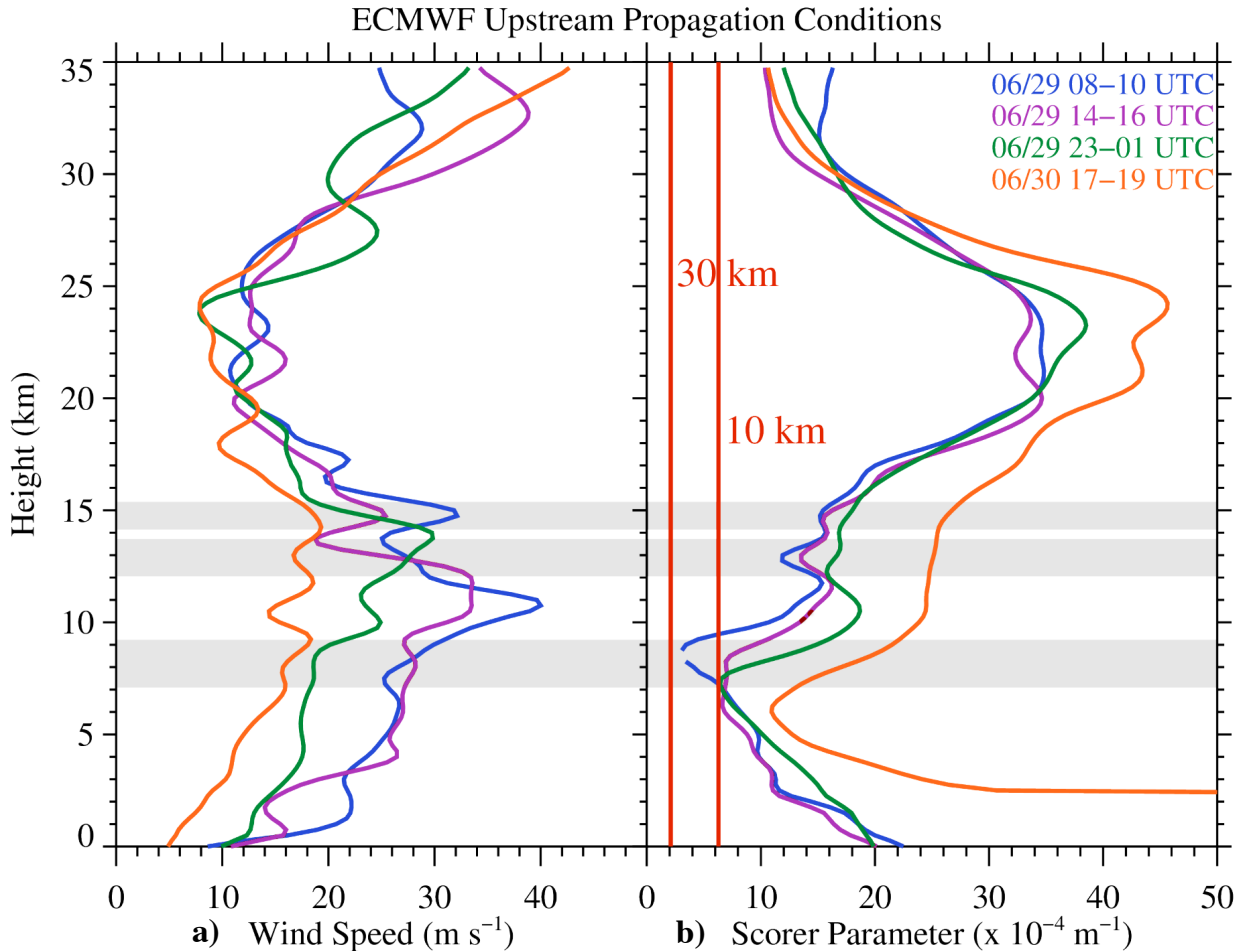
1209 FIG. 5. (a, c, e) ECMWF IFS equivalent potential temperature and (b, d, f) horizontal wind with wind barbs
 1210 and 20-m-spaced contours of geopotential height at 700 hPa for 29 June at 12 UTC, and 30 June 2014 at 00 and
 1211 12 UTC. The transect Mt.-Aspiring-2b is superimposed as black line in the individual panels. The location of
 1212 Mt. Aspiring (MA) is marked with a red dot.



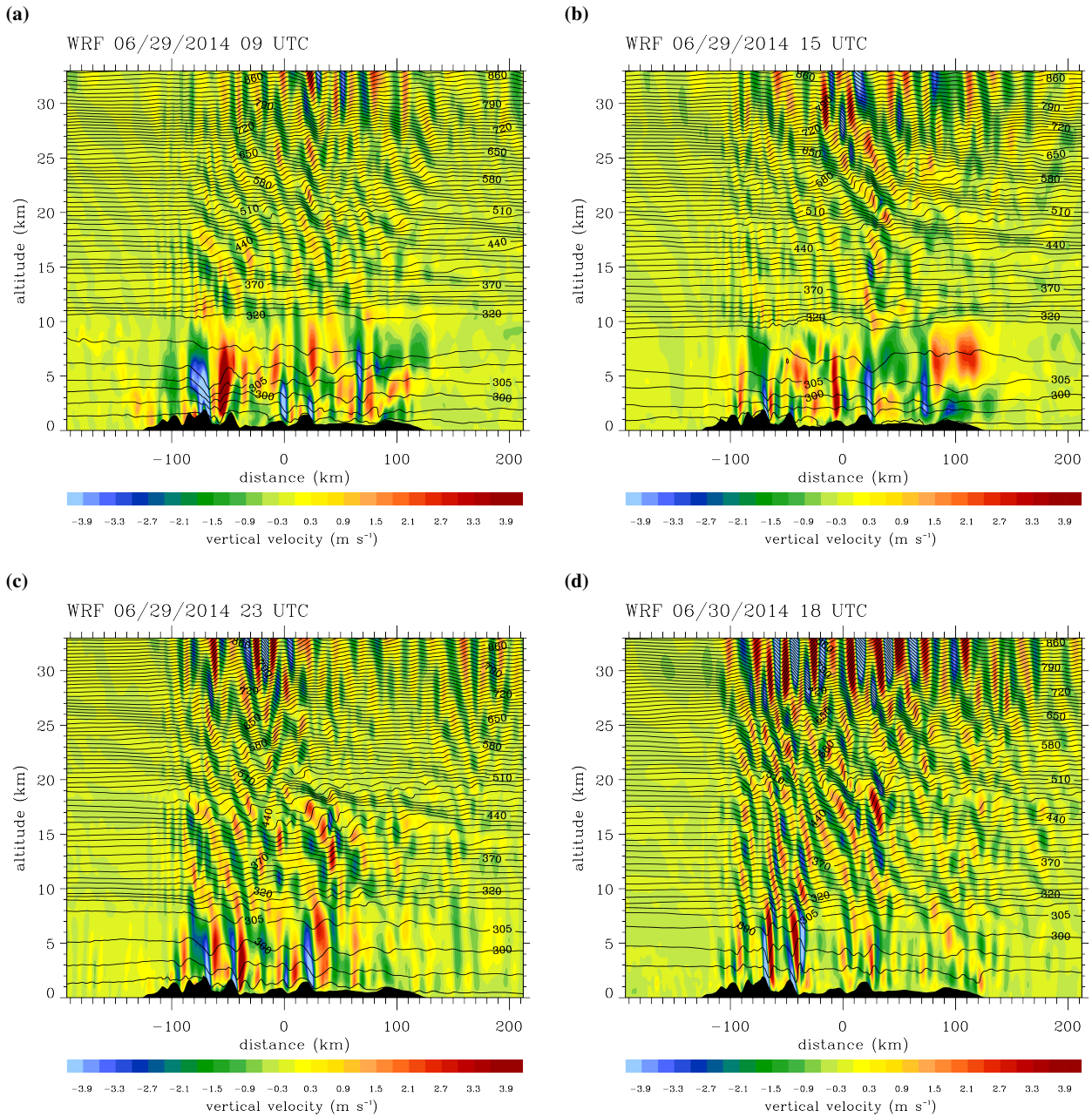
1213 FIG. 6. ECMWF IFS upstream cross-mountain wind speed (at 44.2° S, 167.5° E) during IOP 9 from 00 UTC
 1214 28 June till 06 UTC 01 July 2014. Mean upstream values were calculated as averages over the lowest 4 km
 1215 (blue). Green and orange triangles depict the respective values for the Lauder and Haast sondes. Up to 5 m s^{-1}
 1216 wind speed, the forcing is referred to as “weak”, from 5 to 15 m s^{-1} as “moderate” and more than 15 m s^{-1}
 1217 as “strong”. The dotted-dashed vertical lines refer to the division into accelerating, maximum and decelerating
 1218 forcing. Also periods of synoptic events, like passing fronts and convection are marked. The dashed black curve
 1219 marks an approximation of the transient forcing following $U_{\perp}(t) = U_{\perp 0} + \Delta U_{\perp} \cos^2(\pi t/t_{tot})$ with $U_{\perp 0} = 5 \text{ m s}^{-1}$,
 1220 $\Delta U_{\perp} = 17 \text{ m s}^{-1}$ and $t_{tot} = 53 \text{ h}$.



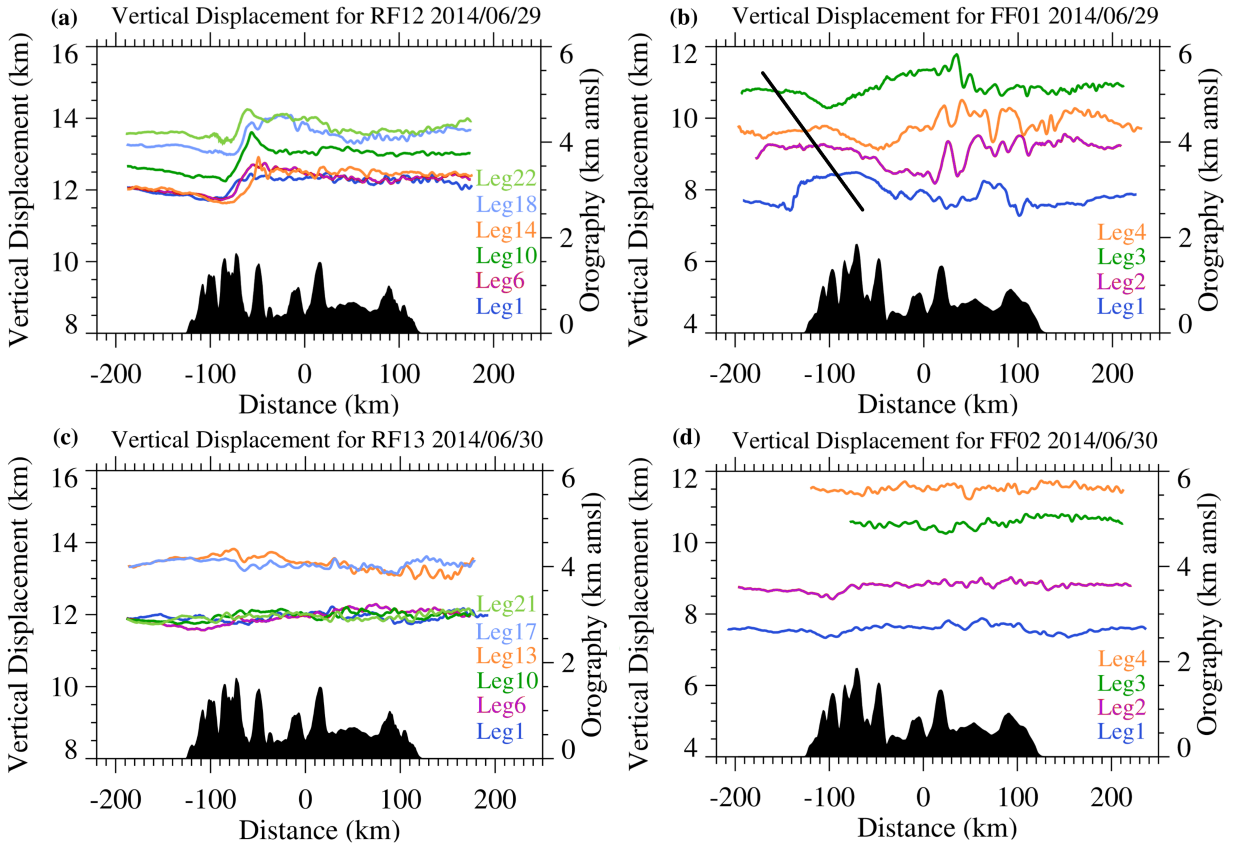
1221 FIG. 7. ECMWF IFS horizontal wind speed with wind barbs and 40-m-spaced contours of geopotential height
 1222 at (a) 300 hPa and (b) 200 hPa at 00 UTC 29 June 2014, (c) 300 hPa and (d) 200 hPa at 00 UTC 30 June 2014,
 1223 (e) 300 hPa and (f) 200 hPa at 12 UTC 30 June 2014.



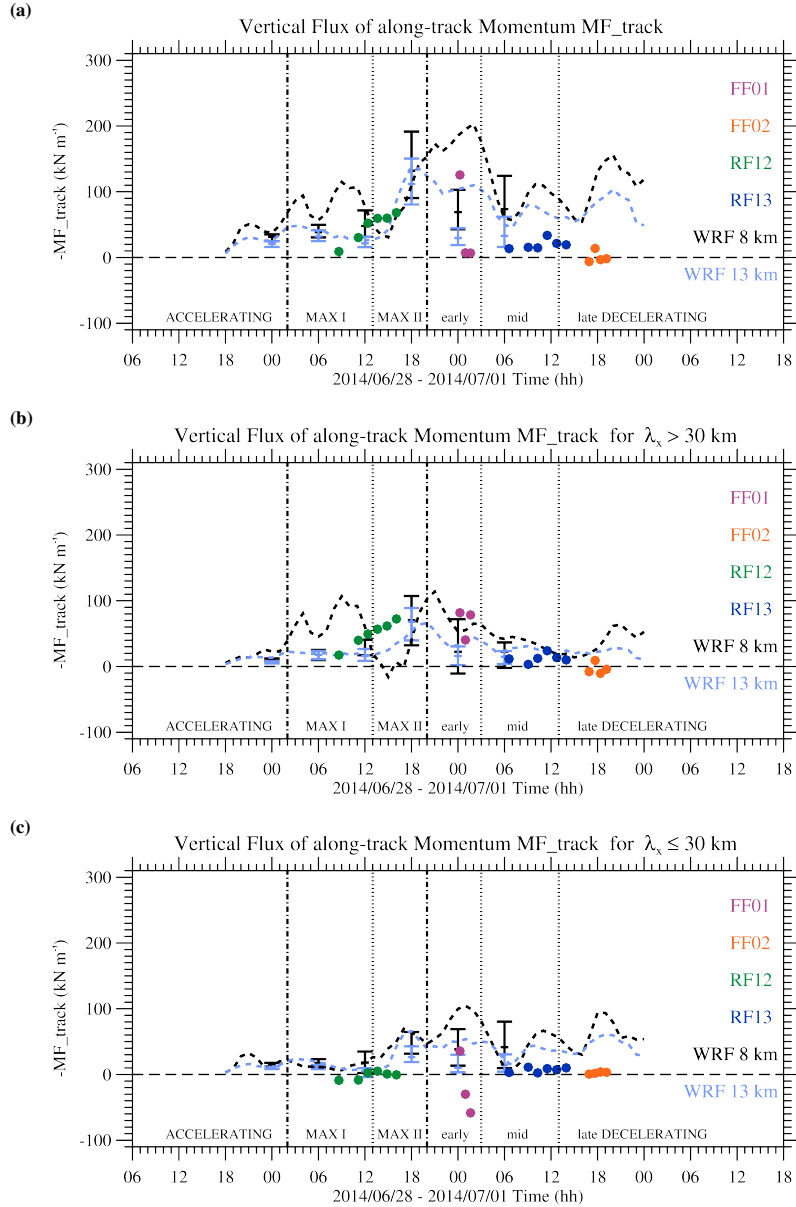
1224 FIG. 8. ECMWF IFS upstream (a) cross-mountain wind speed and (b) Scorer parameter smoothed over 750 m
 1225 in the vertical during 3-hour windows of maximum forcing phase part I (06/29 08 - 10 UTC), part II (06/29 14 -
 1226 16 UTC), early (06/29 23 - 01 UTC) and late (06/30 17 - 19 UTC) decelerating forcing phases. In red, the
 1227 critical wavenumbers and wavelengths for propagation based on an argument from steady-state theory are given
 1228 for different periods (b). Waves are able to propagate as long as the ambient Scorer parameter is larger than the
 1229 selected wavenumber. From bottom to top, the altitude range of inhibited propagation for waves shorter than
 1230 50 km horizontal wavelength during maximum forcing phase part I (06/29 08 - 10 UTC), of strong negative
 1231 shear during maximum forcing phase part II (06/29 14 - 16 UTC) and during early decelerating forcing phase
 1232 (06/29 23 - 01 UTC) are shaded in grey.



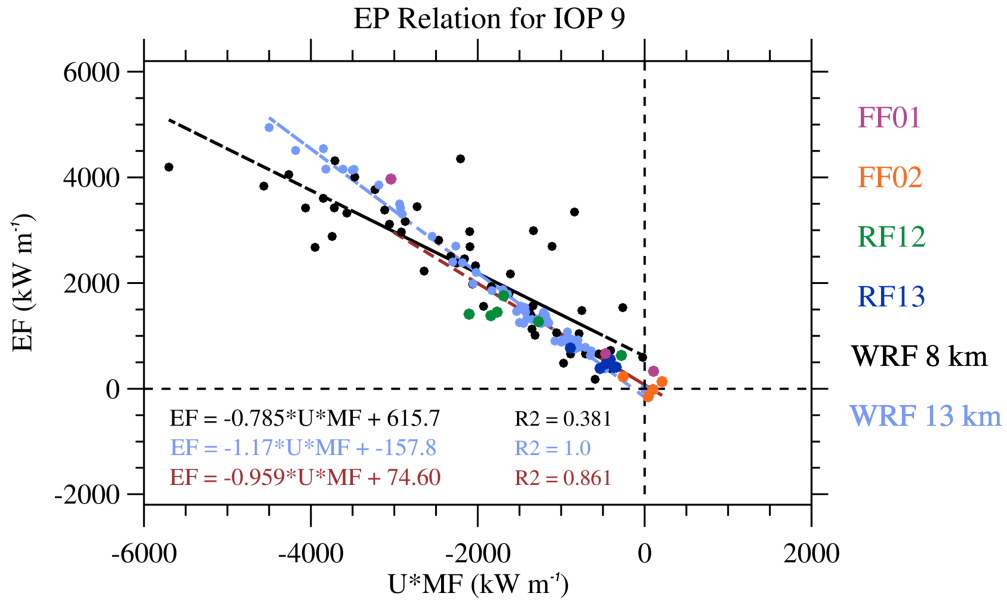
1233 FIG. 9. WRF vertical wind along the Mt.-Aspiring-2b transect up to 33 km altitude (sponge layer is excluded)
 1234 with 5-K-spaced isentropes up to 320 K and 10-K-spaced isentropes above at (a) 09 UTC, (b) 15 UTC, (c) 23
 1235 UTC 29 June and (d) 18 UTC 30 June.



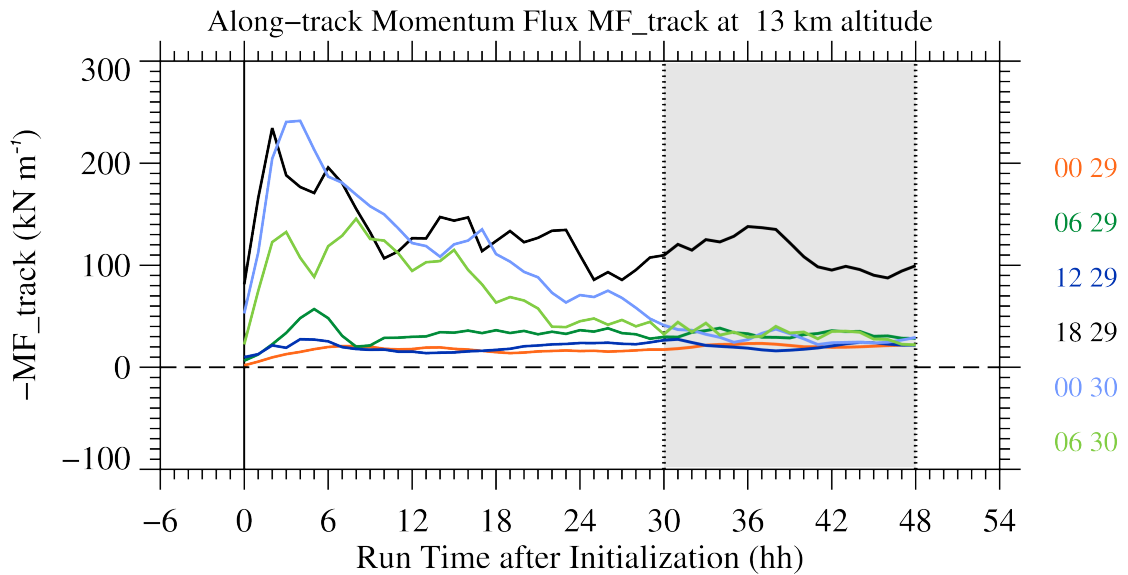
1236 FIG. 10. Vertical displacement for the flight legs of (a) RF12 and (b) FF01 on 29 June 2014, (c) RF13 and (d)
 1237 FF02 on 30 June 2014 with underlying topography along the Mt.-Aspiring-2b transect. For the Falcon legs, the
 1238 topography originates from the WRF model with the finest obtainable resolution of 30 arc seconds. For the GV
 1239 flight tracks, the topographic height was provided by the Earth Observing Laboratory (NCAR EOL). In (b), an
 1240 estimated phase line (black) of the long waves ($\lambda_x \approx 200$ km) is shown to guide the eye.



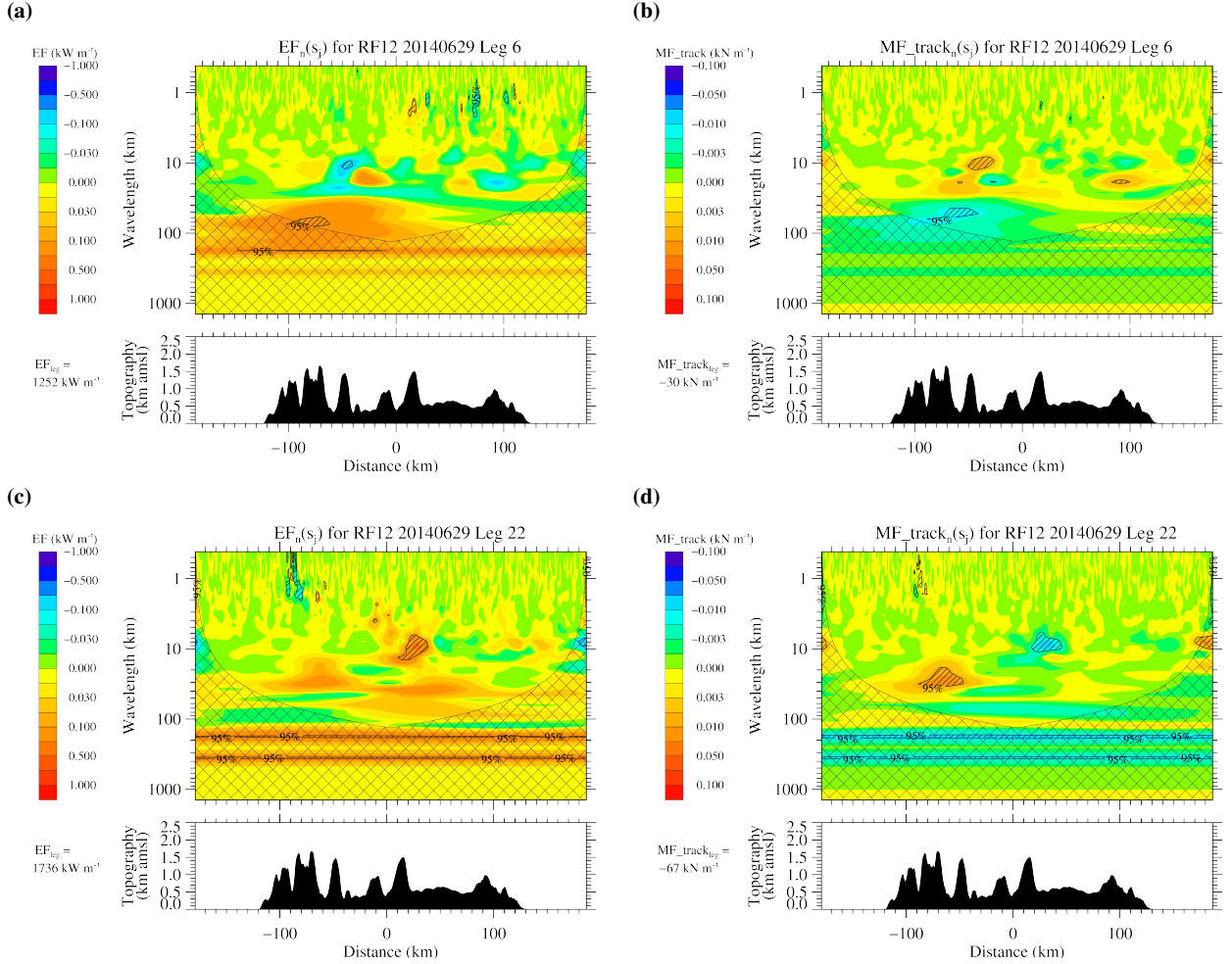
1241 FIG. 11. (a) Time series of leg-integrated vertical flux of along-track momentum ($-MF_{track}$) for the GV
 1242 (RF12 and RF13) and Falcon (FF01 and FF02) aircraft for all Mt.-Aspiring-2b legs, as well as of simulated flux
 1243 values of the WRF model smoothed over 3 h along the Mt.-Aspiring-2b transect at typical flight altitudes of
 1244 8 and 13 km. As in Fig. 2 and 6, the divisions into accelerating, part I and II of maximum, early, mid and late
 1245 decelerating forcing phases are marked with vertical lines. In addition, minimum, mean and maximum $-MF_{track}$ -
 1246 values at 8 (black) and 13 km (light blue) altitude of 6 quasi-steady WRF runs with constant background profiles
 1247 initialized at 00, 06, 12 and 18 UTC on 29 June and at 00 and 06 UTC on 30 June are shown as error bars (also
 1248 see Fig. 13). In (b) and in (c), the same is shown as in (a), but only for signal parts including wavelengths larger
 1249 and smaller than 30 km, respectively.



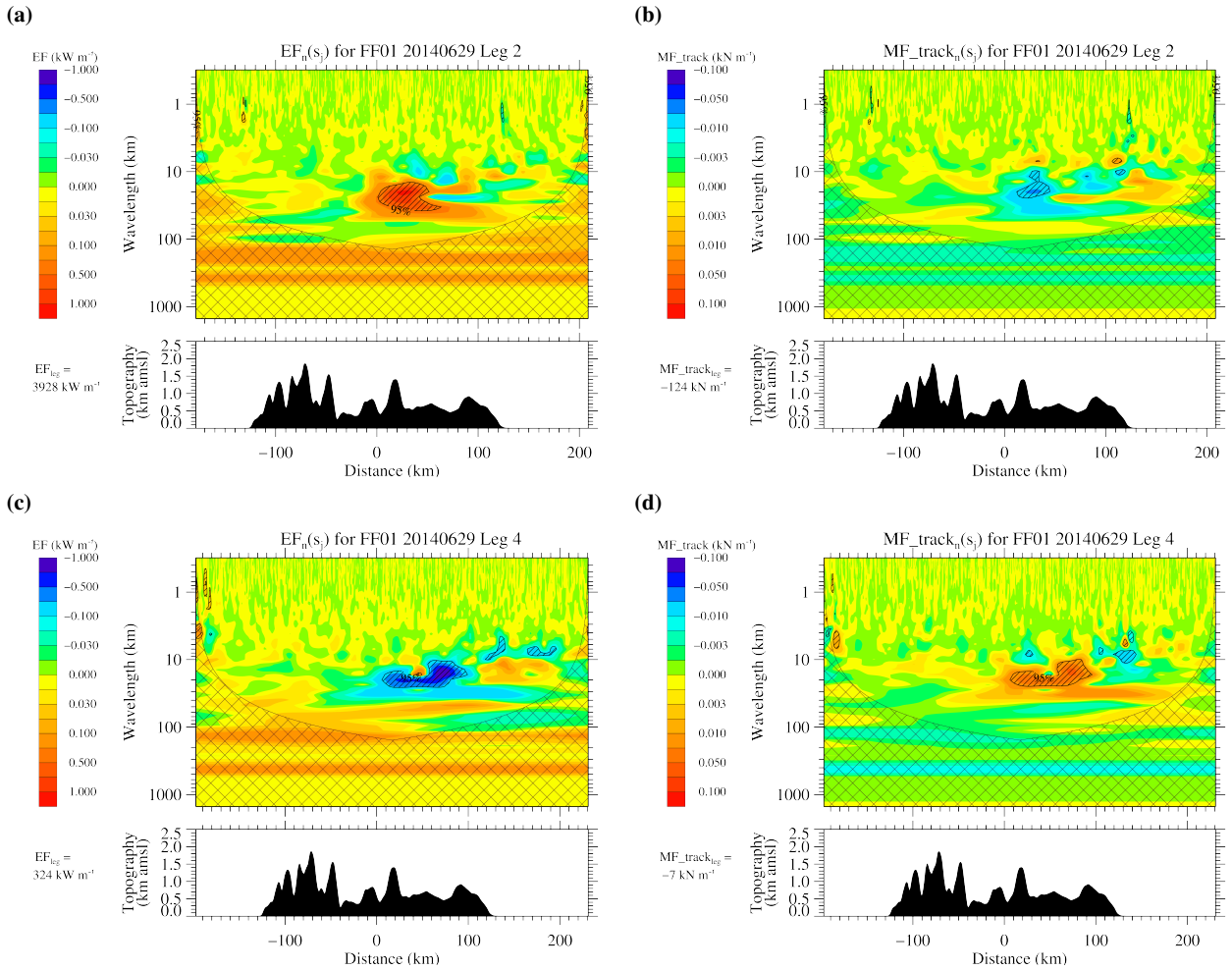
1250 FIG. 12. Test of the linear Eliassen-Palm relation between the energy flux (EF_z) and the scalar product of
 1251 horizontal wind ($\mathbf{U} = [u, v]$) and the horizontal momentum flux ($\mathbf{MF} = [MF_x, MF_y]$) for all Mt.-Aspiring-2b legs
 1252 during IOP 9 and the WRF simulations along the Mt.-Aspiring-2b transect at 8 and 13 km altitude. The solid
 1253 lines represent the linear regression of EF_z and $\mathbf{U} \cdot \mathbf{MF}$ for WRF at 8 km altitude (black), at 13 km altitude (light
 1254 blue) and the airborne observations of the Mt.-Aspiring-2b legs (red). Further given are the respective functions
 1255 of the linear regression and the squared Pearson correlation coefficient R^2 .



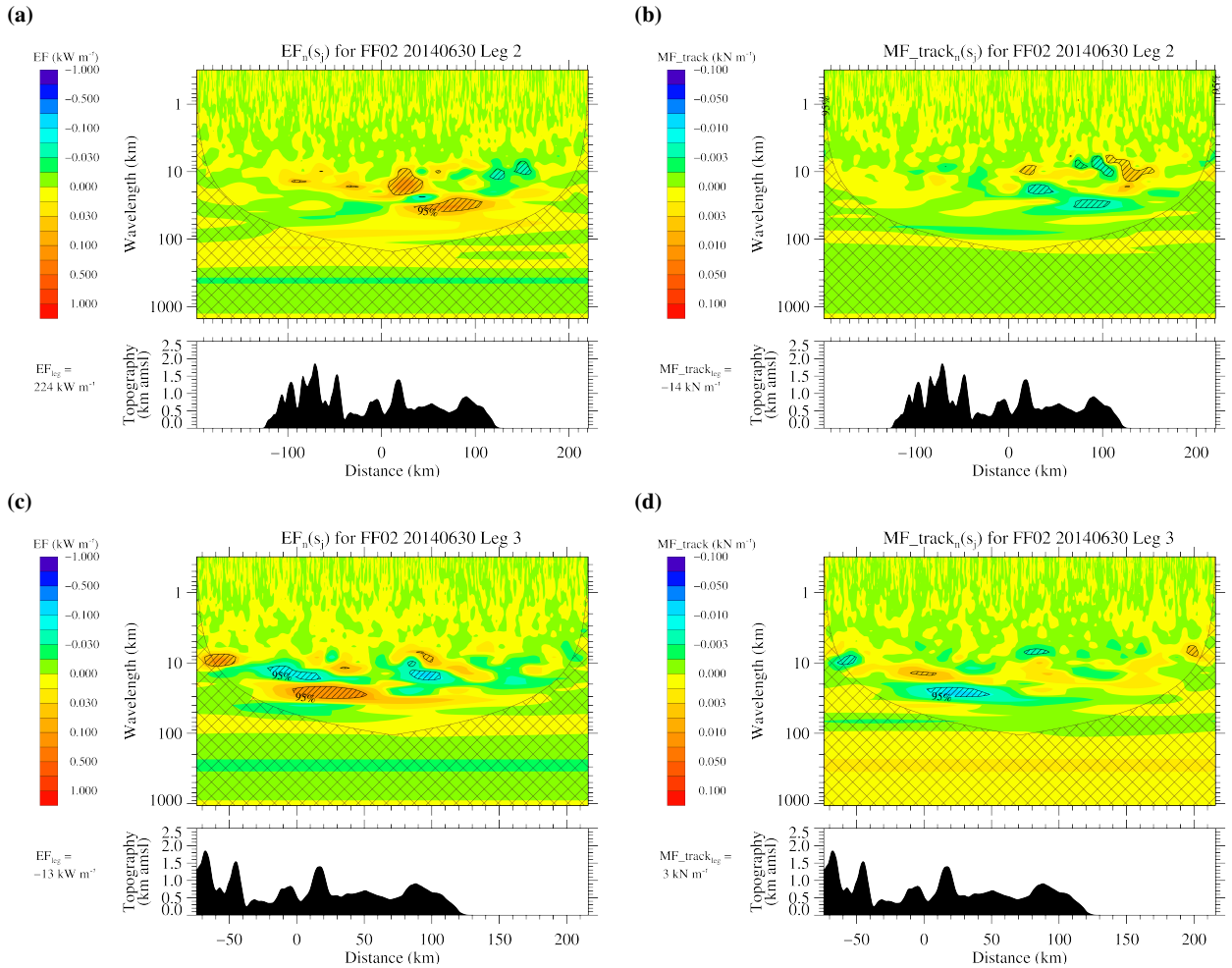
1256 FIG. 13. WRF leg-integrated 3-h-smoothed vertical flux of along-track momentum of quasi-steady runs at
 1257 13 km altitude as a function of run time after the respective initialization. All runs were simulated for 48 hours.
 1258 The light gray shading gives the time interval (30 - 48 hours run time) during which the simulations are as-
 1259 sumed to reach a quasi steady-state. This time interval is used to average the flux values and to compare to the
 1260 “transient” WRF simulation and the observations in Fig. 11.



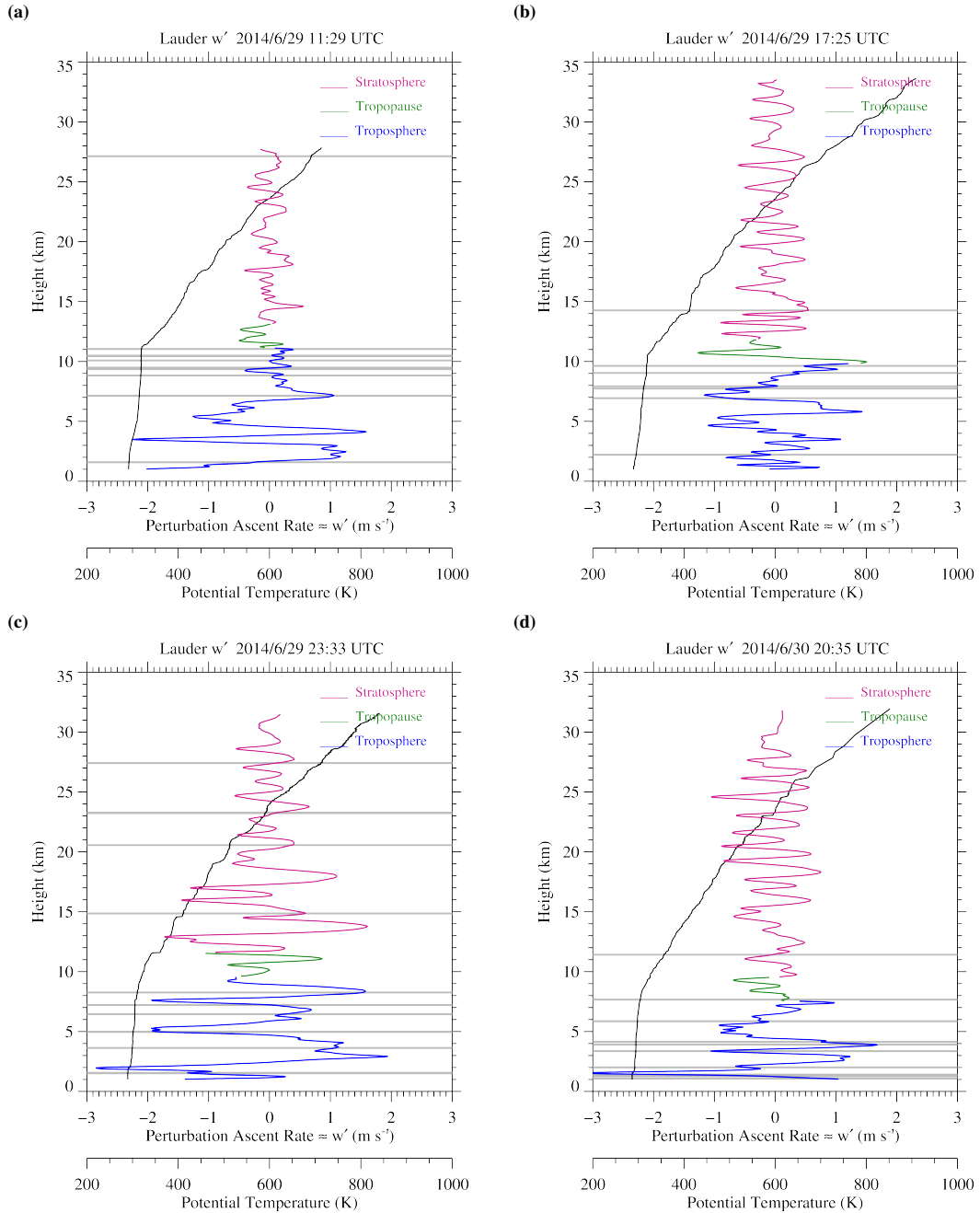
1261 FIG. 14. (a) $EF_{z_n}(s_j)$ (vertical energy flux) and (b) $MF_{\text{track}_n}(s_j)$ (along-track momentum flux) wavelet cospec-
 1262 tra with underlying topography for the GV RF12 leg 6 on 29 June 2014 during maximum forcing phase of the
 1263 IOP 9. The hatched area is significant on the 5%-level and the surrounding solid black line represents the 95%
 1264 confidence limit. The cross-hatched area gives the cone of influence. In (c) and (d) the same is shown as in (a)
 1265 and (b), but for GV RF12 leg 22, respectively.



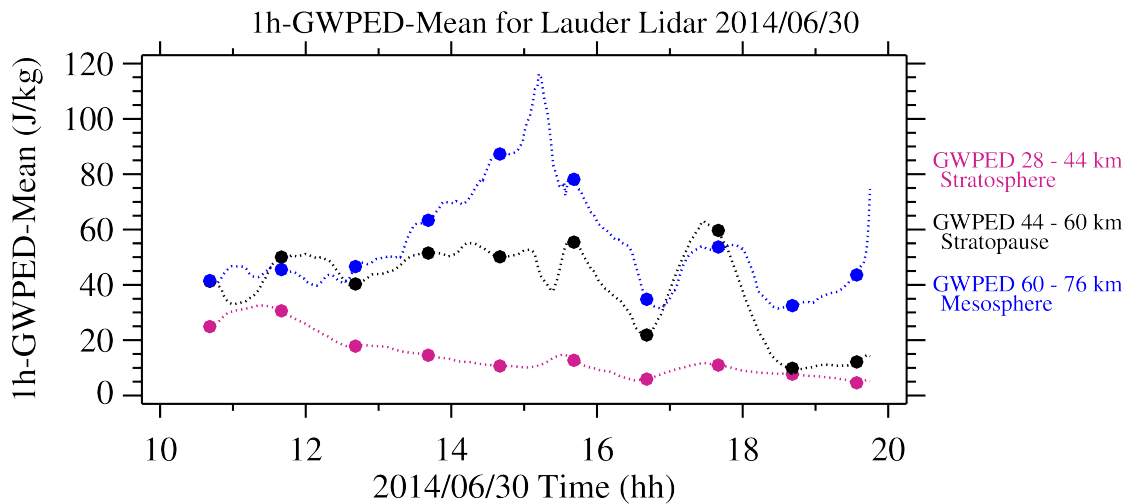
1266 FIG. 15. (a), (b) and (c), (d) same as in Fig. 14a, b but for Falcon FF01 leg 2 on 29 June and leg 4 on 30 June
 1267 2014 during early decelerating forcing phase of the IOP 9.



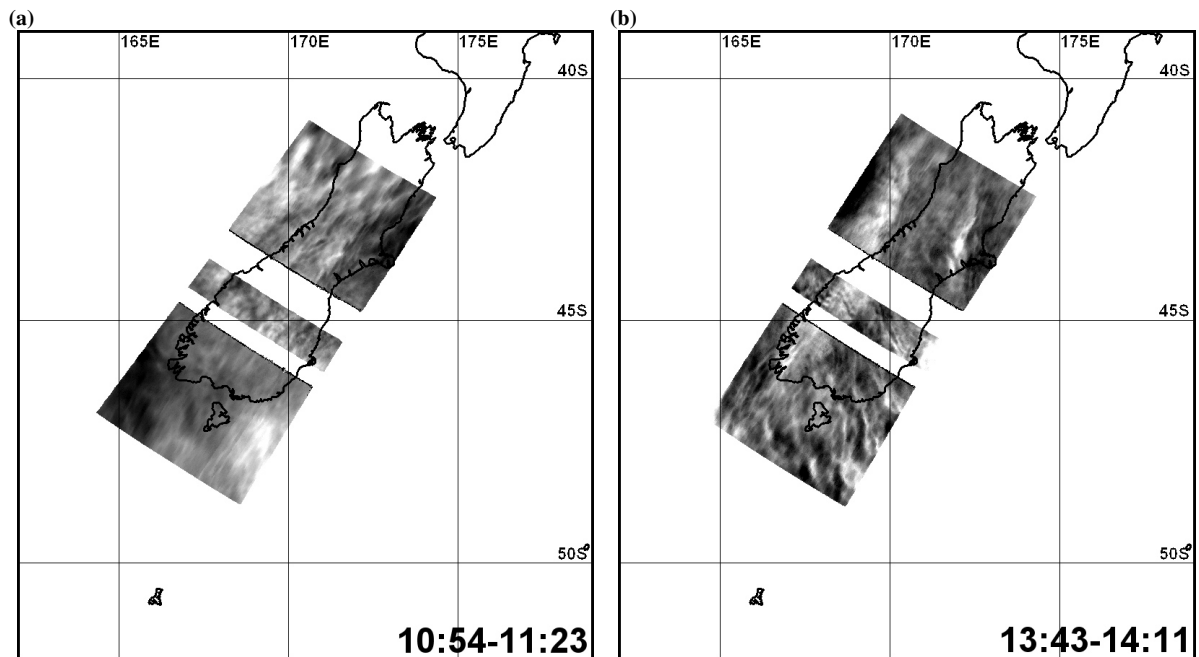
1268 FIG. 16. (a), (b) and (c), (d) same as in Fig. 14a, b but for Falcon FF02 leg 2 and 3 on 30 June during late
 1269 decelerating forcing phase of the IOP 9. Note the different limits of the distance-axis for leg 3 in (c) and (d).



1270 FIG. 17. Density-corrected, approximated vertical velocity fluctuation and potential temperature of the ra-
 1271 diosoundings launched at Lauder on 29 June (a) 11:29 UTC (maximum forcing phase part I), (b) 17:25 UTC
 1272 (maximum forcing phase part II), (c) 23:33 UTC (early decelerating forcing) and on (d) 30 June 20:35 UTC
 1273 (late decelerating forcing). Density-corrected refers to the multiplication of w' by the factor $(\rho(z)/\rho(z=0))^{1/2}$
 1274 to remove the effect of exponentially amplifying w' with height due to decreasing density ρ . The flight passages
 1275 within the troposphere, tropopause and stratosphere are colored in blue, green and violet, respectively. Gray
 1276 shaded are layers where $-0.06 < \partial\theta/\partial z < 0.09 \text{ K km}^{-1}$.



1277 FIG. 18. One-hourly mean of gravity wave potential energy density (GWPED), logarithmically averaged
 1278 over the upper stratosphere (violet dots), stratopause (black dots) and mesosphere (blue dots). In addition,
 1279 the thin dotted lines denote the 1-hourly running mean of the 2-min GWPED data during the Rayleigh lidar
 1280 measurement at Lauder, New Zealand, on 30 June. In general, the GWPED increases with height due to wave
 1281 amplification with decreasing air density.



1282 FIG. 19. Keograms (time-distance sections constructed from collocated time series of narrow AMTM image
 1283 slices) of the AMTM observations during (a) RF12 on 29 June and (b) RF13 on 30 June 2014.